



Magneto-hydrodynamic thermal convection of Cu–Al₂O₃/water hybrid nanofluid saturated with porous media subjected to half-sinusoidal nonuniform heating

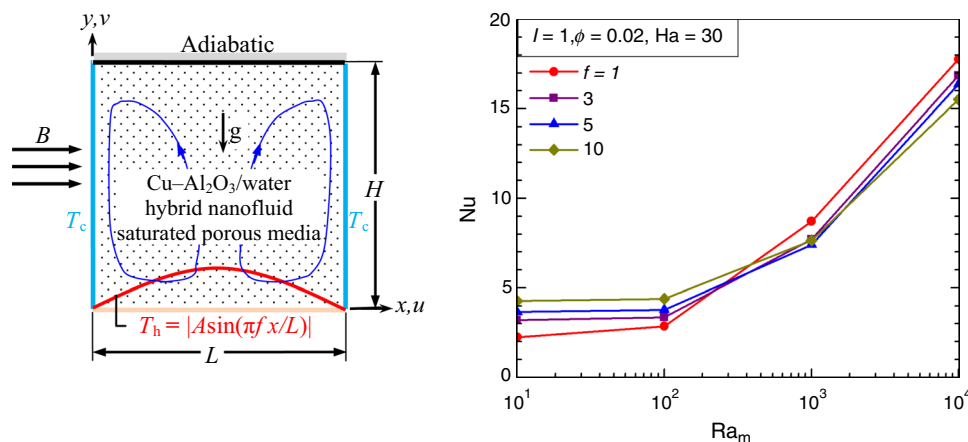
Nirmalendu Biswas¹ · U. K. Sarkar² · Ali J. Chamkha^{3,4} · Nirmal Kumar Manna⁵

Received: 7 April 2020 / Accepted: 24 July 2020 / Published online: 10 August 2020
© Akadémiai Kiadó, Budapest, Hungary 2020

Abstract

The present work aims to examine the thermal efficacy of half-sinusoidal nonuniform heating at different spatial frequencies for a porous natural convection system using Cu–Al₂O₃/water hybrid nanofluid and magnetic field. The system is presented utilizing a classical square enclosure heated nonuniformly at the bottom wall, and the sidewalls are allowed to exchange heat with the surroundings. The Brinkman–Forchheimer–Darcy model is adopted catering other additional terms for buoyant force and magnetic field. The governing equations are transformed into nondimensional forms and then solved numerically using a finite volume-based computing code. The importance and fundamental flow physics are explored in terms of the pertinent parameters such as the amplitude (I) and spatial frequency (f) of half-sinusoidal heating, Darcy–Rayleigh number (Ra_m), volume fraction of hybrid nanoparticles (ϕ), and Hartmann number (Ha). The flow structure and heat transfer characteristics are analyzed and presented utilizing heatlines, streamlines and isotherms and average Nusselt number. The results show that the use of half-sinusoidal nonuniform heating along with hybrid nanofluid can be a viable method for enhancement and control of the overall thermal performance. The study indicates that half-sinusoidal heating could be a promising technique for better heat transfer even in the presence of flow dampening effects like porous media and magnetic fields.

Graphic abstract



Keywords Hybrid nanofluid · Half-sinusoidal heating · Porous cavity · Magneto-hydrodynamics (MHD) · Natural convective heat transfer · Heatlines

✉ Nirmal Kumar Manna
nirmalkmannaju@gmail.com

Extended author information available on the last page of the article

List of symbols

- A Amplitude of sinusoidal heating (K)
- B Magnetic field (Tesla, $N A^{-1} m^{-2}$)
- Da Darcy number

f	Spatial frequency of heating
F_c	Forchheimer coefficient
g	Acceleration due to gravity (m s^{-2})
H	Height of the cavity/length scale (m)
Ha	Hartmann number
I	Dimensionless amplitude of heating
K	Permeability of porous medium (m^2)
L	Length of the cavity (m)
Nu	Average Nusselt number
P	Dimensionless pressure
Pr	Prandtl number
Ra	Fluid Rayleigh number
Ra_m	Darcy–Rayleigh number
T	Temperature (K)
u, v	Velocity components (m s^{-1})
U, V	Dimensionless velocity components
x, y	Cartesian coordinates (m)
X, Y	Dimensionless coordinates

Greek symbols

α	Thermal diffusivity ($\text{m}^2 \text{s}^{-1}$)
β	Thermal expansion coefficient (K^{-1})
ε	Porosity
θ	Dimensionless temperature
μ	Dynamic viscosity ($\text{kg m}^{-1} \text{s}$)
ν	Kinematic viscosity ($\text{m}^2 \text{s}^{-1}$)
ρ	Density (kg m^{-3})
σ	Electrical conductivity (μScm^{-1})
ϕ	Volume fraction of hybrid nanoparticles
ψ	Dimensionless streamfunction
Π	Dimensionless heatfunction

Subscripts

c	Cold
f	Base fluid/liquid
h	Hot
hnf	Hybrid nanofluid
max	Maximum
s	Solid

Introduction

Buoyancy-driven fluid flow and convective heat transfer through the porous substrate is an important topic for research, and it finds numerous engineering applications such as heat exchangers, solar thermal systems, electronic equipment cooling, chemical reactors, management of nuclear waste, geothermal energy systems, energy storage and conservation system, oil and gas processing units, food grain processing units, bio-medical systems. In such applications, the presence of a porous substance (a solid matrix having continuous pores) causes more complex flow physics depending upon the thermal boundary conditions [1–4].

A thorough understanding of thermo-fluid flow behavior within the thermal system is crucial for modeling, designing, and operation of such devices and also a very tricky task for an optimum design by the manufacturer. Researchers are continuously paying their attention for achieving the efficient thermal design through numerical computations [5–8]. Some recent studies depicting the importance of porous media are deliberated toward the technology development [9–13]. These works address thermal analyses carried out experimentally on metallic foam or phase change material embedded with porous substances.

Industrial as well as domestic appliances subjected to temperature gradient face tremendous issues for dissipating the by-product heat (as a result of device operation) in an efficient manner so that the devices can operate within its safe operating temperatures. Thermal management of such a device is a serious challenge to the designer without compromising the efficacy of the device. In this context, the usage of nanofluids, which was first introduced by Choi [14], is a promising approach for improving the thermal conductivity of the working medium. Nanofluids utilize common working fluids/liquids along with dispersed solid particles of nanometer scale. The application of nanofluid has increased significantly even with the critical issues of suspensions and agglomeration of nanoparticles. In general, commonly available base fluids are water, ethylene glycol, bio-fluids, polymer solutions, oils, and lubricants, whereas commonly used nanoparticles are metallic particles of Cu, Al, Fe, Au and Ag, and nonmetallic particles made of CuO , Al_2O_3 , Fe_3O_4 , TiO_2 , and SiC . Researchers have studied various geometrical configurations utilizing different types of nanofluids and reported about the heat transfer augmentation over the conventional base fluids, which is available in the literature [15–21]. Many researchers have also investigated different problems using nanofluids as working media in the presence of magnetic fields [22–25]. Detailed reviews are available in Refs. [26–29].

Although the addition of nanoparticles leads to the improvement in thermal conductivity of base fluids, it involves several issues like erosion due to suspended nanoparticles, pressure drop due to the higher viscosity, increased energy input to pump, flow instability, etc. [30]. The recent technological advancement in the area of heat transfer reveals that the thermal conductivity of conventional fluids (and also mono-nanofluids) can be augmented further by dispersing two or more different types of nanoparticles or their mixture as nanocomposites [30]. When the nanocomposite or individual nanoparticles are added in a suitable base fluid (liquid), it is known as a hybrid nanofluid and it shows better thermal conductivity over the pure base fluid or a mono-nanofluid. Usage of hybrid nanofluids can significantly boost up the thermal performance in numerous applications. Some of the beneficial aspects are documented

in the literature in Refs. [19, 31–33]. However, the hybrid nanofluid shows a higher effective viscosity (particularly when concentration of nanoparticles increases) compared to the conventional fluid and also the mono-nanofluid. It incurs a higher input pumping energy due to reduced flow velocity (as the viscosity increases). The effective properties of hybrid nanofluids depend upon many factors like selection of nanoparticles and their combination, preparation and dispersion techniques, the shape and size of nanoparticles, agglomeration, measuring techniques, etc. In this context, detailed reviews on various aspects of hybrid nanofluids and future scope of further exploitation for potential applications are well documented in Refs. [30, 34, 35].

Suresh et al. [36] experimentally investigated the effects of Cu–Al₂O₃/water hybrid nanofluid and reported ~ 13.56% heat transfer augmentation over the pure water. Utilizing different types of hybrid nanofluids, several researchers have investigated the thermal performance of different complex problems such as MHD convection in a clear domain by Ghalambaz et al. [37], in a porous domain in the absence of magnetic field by Ghalambaz et al. [38], Chamkha et al. [39], and Al-Srayyih et al. [40]. MHD thermal convection of hybrid nanofluids through porous substances has been demonstrated in Refs. [41–46] and in many other works. However, in most of the aforementioned studies, the convective heat transfer characteristics have been investigated using the classical thermal boundary conditions, where heat source has been considered to be either of constant heat flux or constant temperature (isothermal) with some variation in length/position of the heat source. It has been found that, along with the spatially constant thermal boundary condition, as discussed above, the consideration of a nonuniform heating of hybrid nanofluid is also important from fundamentals as well as practical standpoints. For instance, Manna et al. [7] and Biswas et al. [47] have reported the beneficial aspects of a nonuniform heating over the uniform heating of porous media and found about 74–85% heat transfer enhancement. Several other researchers have also investigated the buoyancy-driven convective heat transfer in the porous substances considering a nonuniform sinusoidal heating at the bottom wall [48, 49], horizontal wall(s) [50], or sidewalls [51, 52]. However, the study addressing multi-frequency spatial heating following a half-sinusoidal profile is not attended so far, particularly with any hybrid nanofluid. It motivates to take up the present work using a hybrid nanofluid saturated porous system.

The sinusoidal heating condition has also been studied during natural convective heat transfer of nanofluid through the clear domain by Oztop et al. [53] and Mikhailenko et al. [54], through the porous domain by Alsabery et al. [55] and Arasteh et al. [56]. In other classes of work, the natural convective heat transfer of nanofluid flow through a porous media has been studied considering the effect of cavity shape

like a sinusoidally wavy wall(s) [57–59]. The effect of an external magnetic field on buoyancy-driven thermal convection of nanofluid through porous media under the sinusoidal heating profile has been investigated by Sheremet and Pop [60], Malik and Nayak [61], Nazeer et al. [62], Javaherdeh and Najjarnezami [63], Pordanjani et al. [64], etc. The magneto-hydrodynamic thermal convection of nanomaterial migration in a sinusoidal-shaped porous cavity has been analyzed by Vo et al. [65], whereas Aly and Raizah [66] have investigated MHD convective heat transfer a ferrofluid filled porous cavity heated with a sinusoidal wavy rod.

Recently, enhanced convective heat transfer of hybrid nanofluid, heated sinusoidally, has been investigated by Tayebi and Chamkha [67]. In their study, they found that Cu–Al₂O₃/water hybrid nanofluid has superior heat transfer functionality compared to Al₂O₃/water mono-nanofluid and the base fluid (water). Takabi and Salehi [68] have analyzed the effect of sinusoidal corrugation at the sidewalls of a bottom heated enclosure filled with Cu–Al₂O₃/water hybrid nanofluid. They found that the heat transfer can be improved by adopting hybrid nanofluid compared to a mono-nanofluid. Ashorynejad and Shahriari [69] have studied the MHD convective heat transfer under the combined effect of wavy-walled enclosure, heated sinusoidally at the left side and open at the right side, filled with Cu–Al₂O₃/water hybrid nanofluid. They have reported the positive role of the hybrid nanofluid on the thermal performance of the cavity. Further to the above, the natural convective heat transfer in cavities has also been investigated by many researchers considering hybrid nanofluids as a working media along with [70, 71] or without [72] magnetic fields, or both magnetic fields and porous medium [73–75].

In summary, the selective literature survey clearly points to the importance and usage of sinusoidal heating in engineering applications. It also demonstrates that sinusoidal heating could be a rational approach for improving buoyancy-driven convective heat transfer and can be a powerful controlling means for thermal management. Most of the earlier works have considered a complete cycle of sinusoidal heating (Refs. [7, 47]). However, the present work differs to a great extent from the earlier works. With a complete cycle of the sinusoidal heating profile, one half of the cycle has a less effective role on the heating/convective process as the heat is rejected out though this half cycle. Only the other half cycle of the sinusoidal heating profile participates in the heating/convective process. This causes a loss of input energy or an increased cost of energy investment. Under the circumstances, the use of half-sinusoidal heating profile provides (with the help of proper electrical circuit design and suitable control arrangements) or offers efficient utilization of input energy (can reduce the need of input energy); thus, it enhances heat transfer process for the same work energy investment. In the literature, there exists no

such fundamental analysis. Thus, the outcomes of this present study are very promising and could be helpful to the thermal community for future research and applications in a new direction. In regard to the application of half-sinusoidal heating profile, it could be used in many areas such as electronic components and devices, drying technology, etc. To explore this fact in a better way, the thermal performance of Cu–Al₂O₃/water hybrid nanofluid saturated with porous substrate packed in an enclosure subjected to multi-frequency spatial heating (following a half-sinusoidal function) along with magnetic fields is investigated. Therefore, the outcomes of the present study will contribute to modeling, designing, and development of devices subjected to the thermal applications magnetic fields.

Modeling aspects

The problem of hybrid nanofluid saturated with porous media packed in a two-dimensional square enclosure having length L and height H is presented in Fig. 1a. The bottom wall of the enclosure is heated nonuniformly (by maintaining half-sinusoidal temperature profile, T_h , along x -direction as shown in the figure), whereas the sidewalls are diathermic and kept at a temperature T_c , which is lower than the minimum temperature of the half-sinusoidal temperature profile, T_h , of the bottom wall. Figure 1b illustrates the half-sinusoidal nonuniform temperature profiles for the bottom wall for two values of frequency parameter, $f=1$ and $f=3$. The top wall of the enclosure is thermally insulated. During the computation, the points of singularity at the junctions of hot bottom wall and cold side wall are handled by inserting insulation patches [2] suitably. The no-slip and no-penetration boundary conditions are imposed at all the walls of the enclosure. The gravity force is acting downward as indicated in Fig. 1a. The enclosure is filled with a porous substance saturated with Cu–Al₂O₃/water hybrid nanofluid.

An external magnetic field of strength B is applied along the horizontal direction. It is assumed that the externally applied magnetic field is uniform over the enclosure which is filled with an electrically conducting fluid, and it results in the Lorentz force. The induced magnetic field is neglected; thus, the term representing the applied magnetic field appears in the y -momentum equation. In this study, the Joule heating and the Hall effect are also neglected.

Governing equations in dimensionless forms

The fluid flow and heat transfer inside the enclosure are assumed to be steady, Newtonian, laminar, and incompressible. The density variation in the working fluid is taken care of by the Boussinesq approximation. The porous medium is assumed to be hydrodynamically and thermally homogeneous and isotropic, uniform porosity and permeability throughout the porous domain. The viscous dissipation effect compared to conduction and convection terms in the energy balance equation is assumed to be negligible [1, 7, 8, 18, 76, 77]. Furthermore, the fluid and porous substrate are assumed in the local thermal equilibrium (LTE) condition [8, 47, 76, 77]. In this study, the hybrid nanofluid is modeled as a single-phase homogeneous fluid, whereas it is the mixture (at different proportions) of two different nanoparticles Cu and Al₂O₃ is dispersed in pure fluid (water). The nanoparticles are assumed to be uniform in size and are spherical in shape; the diameter of nanoparticles is in the order of ~ 1 nm. The nanoparticles are stable for all time and suspended homogeneously in the pure fluid without any sedimentation or agglomeration [68, 69]. In the present simulation, the thermophysical properties of the pure fluid ($Pr=6.93$) as well as the nanoparticles (of Cu and Al₂O₃) are taken as constant assuming an average fluid temperature of 300 K [77–79], which are listed in Table 1. The modeling of hybrid nanofluid flow through the porous media is executed following the above assumptions and adopting

Fig. 1 (Color figure online) a Schematic diagram of the physical domain packed with hybrid nanofluid saturated with porous media along with boundary conditions, b half-sinusoidal nonuniform temperature profiles for the heating along the bottom wall

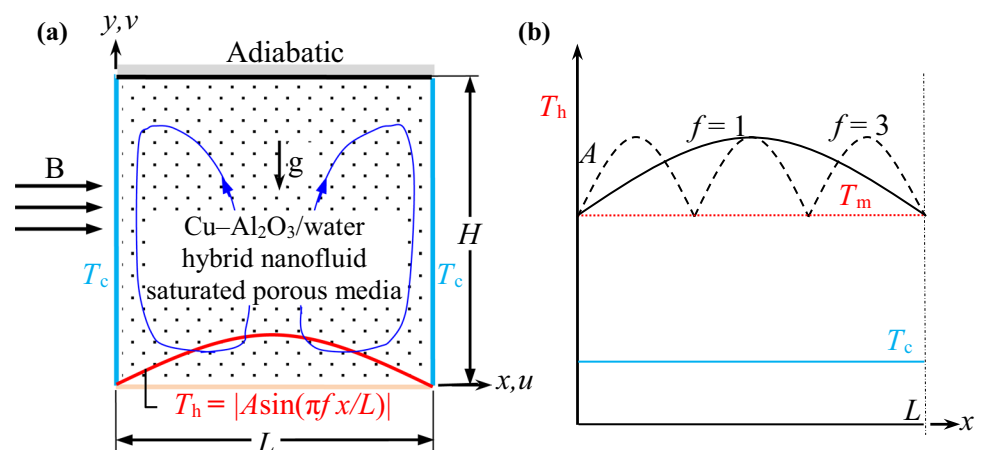


Table 1 Thermophysical properties of water, Cu, and Al₂O₃ [36, 37, 39, 41]

Physical properties	Water	Cu	Al ₂ O ₃
$c_p/J\text{ kg}^{-1}\text{ K}^{-1}$	4179	385	765
$k/W\text{ m}^{-1}\text{ K}^{-1}$	0.613	401	40
$\alpha/kg\text{ m}^{-3}$	1.47×10^{-7}	1.11×10^{-4}	131.7×10^{-7}
β/K^{-1}	21×10^{-5}	1.67×10^{-5}	0.85×10^{-5}
$\rho/kg\text{ m}^{-3}$	997.1	8933	3970
$\mu/kg\text{ m}^{-1}\text{ s}^{-1}$	9.09×10^{-4}	–	–

the Brinkman–Forchheimer–Darcy model [3, 5]. This model addresses the resistive force fluid experiencing when passing through a porous medium. The resulting dimensional partial differential equations (PDEs) for mass, momentum, and energy equation can be written as [43, 61]

$$\frac{\partial u}{\partial x} + \frac{\partial v}{\partial y} = 0 \tag{1}$$

$$\frac{1}{\epsilon^2} \left(u \frac{\partial u}{\partial x} + v \frac{\partial u}{\partial y} \right) = -\frac{1}{\rho_{hnf}} \frac{\partial p}{\partial x} + \frac{v_{hnf}}{\epsilon} \left(\frac{\partial^2 u}{\partial x^2} + \frac{\partial^2 u}{\partial y^2} \right) - \left(\frac{v_{hnf}}{K} u + \frac{F_c}{\sqrt{K}} u \sqrt{u^2 + v^2} \right) \tag{2}$$

$$\frac{1}{\epsilon^2} \left(u \frac{\partial v}{\partial x} + v \frac{\partial v}{\partial y} \right) = -\frac{1}{\rho_{hnf}} \frac{\partial p}{\partial y} + \frac{v_{hnf}}{\epsilon} \left(\frac{\partial^2 v}{\partial x^2} + \frac{\partial^2 v}{\partial y^2} \right) - \left(\frac{v_{hnf}}{K} v + \frac{F_c}{\sqrt{K}} v \sqrt{u^2 + v^2} \right) - \frac{1}{\rho_{hnf}} \sigma_{hnf} B^2 v + \frac{(\rho\beta)_{hnf}}{\rho_{hnf}} g(T - T_c) \tag{3}$$

$$u \frac{\partial T}{\partial x} + v \frac{\partial T}{\partial y} = \alpha_{hnf} \left(\frac{\partial^2 T}{\partial x^2} + \frac{\partial^2 T}{\partial y^2} \right) \tag{4}$$

Equations (2) and (3) indicate the Brinkman–Forchheimer–Darcy model for a buoyancy-driven flow in the presence of a magnetic field. The last two terms of Eq. (3) are due to magnetic force (involving σ) and buoyant force (involving g).

The above dimensional equations are modified into dimensionless forms for the purpose of this present investigation as

$$\frac{\partial U}{\partial X} + \frac{\partial V}{\partial Y} = 0 \tag{5}$$

$$\frac{1}{\epsilon^2} \left(U \frac{\partial U}{\partial X} + V \frac{\partial U}{\partial Y} \right) = -\frac{\rho_f}{\rho_{hnf}} \frac{\partial P}{\partial X} + \frac{v_{hnf} Pr}{v_f \epsilon} \left(\frac{\partial^2 U}{\partial X^2} + \frac{\partial^2 U}{\partial Y^2} \right) - \left(\frac{v_{hnf} Pr}{v_f Da} + \frac{F_c \sqrt{U^2 + V^2}}{\sqrt{Da} \epsilon^{3/2}} \right) U \tag{6}$$

$$\frac{1}{\epsilon^2} \left(U \frac{\partial V}{\partial X} + V \frac{\partial V}{\partial Y} \right) = -\frac{\rho_f}{\rho_{hnf}} \frac{\partial P}{\partial Y} + \frac{v_{hnf} Pr}{v_f \epsilon} \left(\frac{\partial^2 V}{\partial X^2} + \frac{\partial^2 V}{\partial Y^2} \right) - \left(\frac{v_{hnf} Pr}{v_f Da} + \frac{F_c \sqrt{U^2 + V^2}}{\sqrt{Da} \epsilon^{3/2}} \right) V - \frac{\rho_f}{\rho_{hnf}} \frac{\sigma_{hnf}}{\sigma_f} Ha^2 V + \frac{(\rho\beta)_{hnf}}{\rho_{hnf} \beta_f} Ra Pr \theta \tag{7}$$

$$\left(U \frac{\partial \theta}{\partial X} + V \frac{\partial \theta}{\partial Y} \right) = \frac{\alpha_{hnf}}{\alpha_f} \left(\frac{\partial^2 \theta}{\partial X^2} + \frac{\partial^2 \theta}{\partial Y^2} \right) \tag{8}$$

The symbols α_f , β_f , v_f , ρ_f and σ_f indicate, respectively, the thermal diffusivity, volumetric thermal expansion coefficient, kinematic viscosity, density, and electrical conductivity of the base fluid. The above nondimensional governing Eqs. (5)–(8) are obtained using the following dimensionless variables

$$(X, Y) = (x, y)/H; (U, V) = (u, v)H/\alpha_f; \theta = (T - T_c)/(T_m - T_c); P = (p - p_a)H^2/\rho_f \alpha_f^2 \tag{9a}$$

$$Pr = \frac{v_f}{\alpha_f}; \quad Da = \frac{K}{H^2}; \quad F_c = \frac{1.75}{\sqrt{150}}; \tag{9b}$$

$$Ra = \frac{g\beta_f(T_m - T_c)H^3}{v_f \alpha_f}; \quad Ra_m = Ra Da; \quad Ha = \frac{BH}{\sqrt{v_f \rho_f / \sigma_f}} \tag{9b}$$

where the dimensionless numbers are Rayleigh number (Ra), Darcy–Rayleigh number (Ra_m), Prandtl number (Pr), Darcy number (Da), Hartmann number (Ha), and Forchheimer coefficient (F_c). The symbol T_m denotes the mean temperature of heating.

Thermophysical properties of hybrid nanofluid

In the dimensionless governing Eqs. (5)–(8), U and V are the velocity components in dimensionless coordinates in X and Y directions, θ is nondimensional temperature, P is nondimensional fluid pressure, ϵ is the porosity of porous media, and g is the acceleration due to gravity. The thermophysical properties are presented by the subscript ‘‘hnf’’ for the hybrid nanofluid. All these properties are estimated on the basis of a mixture of Cu and Al₂O₃ hybrid nanoparticles volumetric concentration (ϕ) in the pure fluid, so that

$$\phi = \phi_{Al_2O_3} + \phi_{Cu} \tag{10}$$

The subscripts ‘‘f’’ and ‘‘s’’ are utilized for denoting the thermophysical properties for the pure fluid and the solid nanoparticles, respectively.

The effective density ρ_{hnf} , specific heat capacity $(c_p)_{hnf}$, thermal expansion coefficient β_{hnf} of the hybrid nanofluid are expressed by [37, 39, 40, 43]

$$\rho_{hnf} = (1 - \phi)\rho_f + \phi_{Al_2O_3}\rho_{Al_2O_3} + \phi_{Cu}\rho_{Cu} \tag{11}$$

$$(\rho c_p)_{hnf} = (1 - \phi)(\rho c_p)_f + \phi_{Al_2O_3}(\rho c_p)_{Al_2O_3} + \phi_{Cu}(\rho c_p)_{Cu} \tag{12}$$

$$(\rho\beta)_{hnf} = (1 - \phi)(\rho\beta)_f + \phi_{Al_2O_3}(\rho\beta)_{Al_2O_3} + \phi_{Cu}(\rho\beta)_{Cu} \tag{13}$$

The hybrid nanofluid thermal diffusivity is expressed as

$$\alpha_{hnf} = \frac{k_{hnf}}{(\rho c_p)_{hnf}} \tag{14}$$

The effective dynamic viscosity of the hybrid nanofluid is expressed following the classical Brinkman model [79] as:

$$\mu_{hnf} = \frac{\mu_f}{(1 - \phi)^{2.5}} \tag{15}$$

Furthermore, the effective electrical conductivity of the hybrid nanofluid is calculated following the Maxwell model [80]

$$\sigma_{hnf} = \sigma_f \left[1 + \frac{3(\sigma_s/\sigma_f - 1)\phi}{(\sigma_s/\sigma_f + 2) - (\sigma_s/\sigma_f - 1)\phi} \right] \tag{16a}$$

where

$$\phi\sigma_s = \phi_{Cu}\sigma_{Cu} + \phi_{Al_2O_3}\sigma_{Al_2O_3} \tag{16b}$$

The effective thermal conductivity could be obtained by the Maxwell model [80] as

$$k_{hnf} = k_f \left[\frac{(k_s + 2k_f) - 2\phi(k_f - k_s)}{(k_s + 2k_f) + \phi(k_f - k_s)} \right] \tag{17a}$$

where

$$\phi k_s = \phi_{Cu}k_{Cu} + \phi_{Al_2O_3}k_{Al_2O_3} \tag{17b}$$

In the above equations, the thermal conductivities of Cu and Al₂O₃ and the pure fluid nanoparticles are expressed as k_{Cu} , $k_{Al_2O_3}$, and k_f , respectively. Such expressions have been used by many researchers as reported in the published literature. However, in reality, such classical models fail to accurately estimate the thermal conductivity (Maxwell model) as well as viscosity (Brinkman model) of the Cu–Al₂O₃/water hybrid nanofluid [36, 37, 39, 41, 81]. In order to get the correct effective thermal conductivity and viscosity for the

hybrid nanofluid, the available experimental data [36] are utilized in the present study, which are tabulated in Table 2 for $\phi = 0.001\text{--}0.02$. However, for extending the present numerical study, we have extrapolated the data little bit for a range of hybrid nanoparticles volume fraction $\phi = 0.03\text{--}0.05$, which are indicated in the last three rows of Table 2.

The overall heat transfer characteristics, the quantity of physical interest, are evaluated by calculating the average Nusselt number (Nu) at the bottom heated wall, which can be written as

$$Nu = \frac{k_{hnf}}{k_f} \int_0^1 \left(-\frac{\partial\theta}{\partial Y} \Big|_{Y=0} \right) dX \tag{18}$$

Furthermore, the fluid flow structure within the computational domain is visualized by mapping the contours of streamlines. It is generated by using streamfunction ψ and expressed through

$$-\frac{\partial\psi}{\partial X} = V \quad \text{and} \quad \frac{\partial\psi}{\partial Y} = U \tag{19}$$

At all the walls of the enclosure, ψ is zero. The presence of circular streamlines in a confined cavity/enclosure is very important to understand the associated flow physics. The circular streamlines indicate a rotating fluid flow usually mentioned as vortex or circulation. The presence of the circulation in a confined cavity like the present problem brings out many important flow physics under different parametric (as well as boundary) conditions. The location, strength, and size and shape of the circulation decide the local transport behavior of a undergoing process which may involve heat transfer and other transport phenomena. In general, ‘‘+ ψ ’’ indicates counterclockwise (CCW) fluid circulation and ‘‘– ψ ’’ indicates clockwise (CW) fluid circulation. The congested streamlines imply a stronger fluid velocity between the bounding streamlines. If the distance between the two successive streamlines is higher, the flow velocity becomes

Table 2 Effective thermal conductivity and dynamic viscosity [36] of Cu–Al₂O₃/water hybrid nanofluid

$\phi/\%$	$\phi_{Cu}/\%$	$\phi_{Al_2O_3}/\%$	$k_{hnf}/W\ m^{-1}\ K^{-1}$	$\mu_{hnf}/kg\ m^{-1}\ s^{-1}$
0.1	0.0038	0.0962	0.619982	0.000972
0.33	0.0125	0.3175	0.630980	0.001098
0.75	0.0285	0.7215	0.649004	0.001386
1.0	0.0380	0.9620	0.657008	0.001602
2.0	0.0759	1.9241	0.684992	0.001935
3.0	0.1138	2.8862	0.712976	0.002268
4.0	0.1517	3.8483	0.712976	0.002268
5.0	0.1896	4.8104	0.740960	0.002601

lower due to a wider flow area as per the mass balance/continuity equation.

Further to the above, the transport of thermal energy from the heated bottom wall to the cold sidewalls is visualized by mapping the contours of heatlines. The heatlines are basically obtained from the energy balance at the steady-state condition, and it is generated from the heatfunction (Π) [7, 47, 82], which can be expressed as

$$-\frac{\partial \Pi}{\partial X} = V\theta - \frac{\partial \theta}{\partial Y} \quad \text{and} \quad \frac{\partial \Pi}{\partial Y} = U\theta - \frac{\partial \theta}{\partial X} \quad (20)$$

The above equations are solved in an integration approach considering the Dirichlet and Neumann boundary conditions for the temperature and zero surface velocity. At the beginning, the solution is started by setting a reference point for the Π by setting as “0” at the central point of the bottom wall ($X=0.5, Y=0$); this also ensures a symmetrical pattern of the heatlines contours.

Boundary conditions for the computation

The dimensionless governing Eqs. (5)–(8) by applying the following boundary conditions:

- $U=V=0, \theta = |I \sin(\pi f X)|$ for the heated bottom wall ($Y=0$),
- $U=V=\frac{\partial \theta}{\partial Y} = 0$ for the top adiabatic wall ($Y=1$),
- $U=V=0, \theta = 0$ for the cold sidewalls ($X=0,1$),

where the symbol I denotes the dimensionless amplitude [$I=A/(T_m - T_c)$] of half-sinusoidal heating (temperature) profile and it can vary in between 0.1 and 1, whereas f stands for multi-frequency of half-sinusoidal heating (temperature) and it varies from 1 to 10 in this study.

Numerical procedure, grid independence test, and validation study

The dimensionless forms of the coupled nonlinear partial differential conservation Eqs. (5)–(8) along with the applied boundary conditions are transformed into a set of algebraic equations following the finite volume approach (FVM). The second-order central difference scheme for the diffusion terms and QUICK (a third-order upwind differencing scheme) for the advection terms are adopted during the discretization of the governing equations. Finally, the algebraic equations are solved following an iterative process through the Alternate Direction Implicit (ADI) sweep and the TDMA algorithm, invoking the SIMPLE algorithm [81]. The iterative solutions of the governing equations are achieved through the progressive minimization of the normalized residuals of the mass, momentum, and temperature

equations. As the convergence criteria, the cutoff value is set for all residuals $< 10^{-8}$. For a higher level of accuracy, the mass defect of the continuity equation of individual computing cells is also checked, which is set below 10^{-10} . To achieve the required convergence, the values of underrelaxation factors are taken as 0.5, 1.0, and 0.7 for the velocity, pressure, and temperature, respectively. The whole numerical process is carried out using an indigenous FORTRAN computing CFD code.

Code validation

The indigenously developed computing code has already been validated in our earlier works on natural convection [7, 77, 82, 83], mixed convection [76, 84] problems. Furthermore, one new validation study of magneto-hydrodynamic natural convection is conducted here using a Al₂O₃-water nanofluid filled differentially heated cavity as reported by Ghasemi et al. [85]. The present set of governing equations is utilized as a special case by dropping the Darcy and Forchheimer terms (for porous medium) and setting porosity $\varepsilon = 1$. The same set of governing equations and constitutive relations is utilized by setting $\phi_{Cu} = 0$. It turns the governing equations shown for the hybrid nanofluid flow (consisting of two different nanoparticles) into the governing equations for the nanofluid flow of Al₂O₃/water.

The results of contour maps on streamlines and isotherms for $Pr = 6.2, Ra = 10^5, Ha = 60$, and nanoparticles volume fractions $\phi_{Al_2O_3} = 0.03$ are compared and illustrated in Fig. 2 (first row) and are found to be closer with the present simulated results (second row). The comparison of our results

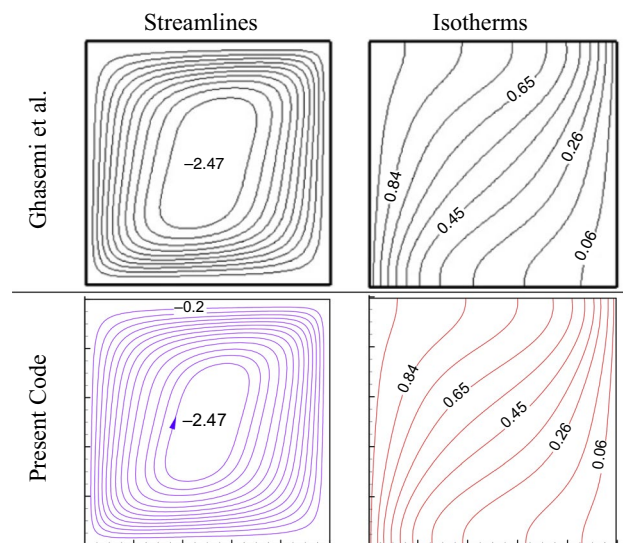


Fig. 2 (Color figure online) Comparison of streamlines and isotherms contours maps of a differentially heated cavity with $Pr = 6.2, Ra = 10^5, Ha = 60, \phi_{Al_2O_3} = 0.03$ of present results with those of the benchmark problem of Ghasemi et al. [85]

and those reported in the published literature [85] shows reasonable good agreement. Based on the reported earlier validations [7, 76, 77, 82–84] and this new validation, it is clear that the reliability and accuracy of the present computing code are satisfactory to carry out the numerical simulations.

Grid independence study

For ensuring the numerical results to be independent of the number of meshes, a grid independence test is conducted using the five different grid sizes (80×80 , 120×120 , 160×160 , 200×200 , and 250×250). The uniform structured grid is distributed over the computational domain. To compare different mesh results, the average Nusselt number (Nu) is computed at the bottom wall ($Y=0$) for different Darcy–Rayleigh numbers ($Ra_m = 10-10^4$) for the fixed values of $Da = 10^{-4}$, $\varepsilon = 0.6$, $I = 1$, $f = 5$, $Ha = 30$. The same is presented in Table 3. The successive errors in the estimation of the average Nu (as indicated in % in bracket) are compared with the immediate coarse grids, and it is found to be $< 1.1\%$ with 200×200 grid size. There is no significant change in the average Nu value beyond the grid size 200×200 . Accordingly, 200×200 grid size is used throughout the numerical analysis of the studied problem.

Results and discussion

The effect of multi-frequency half-sinusoidal heating of Cu–Al₂O₃/water hybrid nanofluid saturated with porous medium in a square cavity in presence of external magnetic field is analyzed numerically. The effect of different parametric variations on the thermo-flow physics is illustrated through the streamlines and isotherms. Heat energy transportation from the heat source to the heat sink is visualized using Bejan’s heatlines. Overall heat transfer characteristics under various selected effective parameters are presented in terms of the average Nusselt number (Nu). The analysis of the porous media is carried out for the variation in Darcy–Rayleigh number $Ra_m = 10, 10^2, 10^3, 10^4$, Darcy number $Da = 10^{-5}, 10^{-4}, 10^{-3}, 10^{-2}, 10^{-1}$ keeping the fixed values of porosity $\varepsilon = 0.6$. Whereas the multi-frequency half-sinusoidal heating is analyzed by varying the amplitude as $I = 0.05, 0.3, 0.5, 0.8, 1$, the frequency

of half-sinusoidal heating is varied as $f = 1, 3, 5, 7, 10$. The concentration of Cu–Al₂O₃/water hybrid nanofluid is varied as $\phi = 0.001-0.05$. The strength of the externally applied magnetic field is varied as $Ha = 0, 10, 30$, and 50 . All the results are presented in “Effect of operating convection regimes (Ra_m)”–“Influence of varying frequency (f) of half-sinusoidal heating” sections. Firstly, the effect of operating convection regimes varying Darcy–Rayleigh numbers on the thermo-fluid flow structure under the multi-frequency half-sinusoidal heating is presented in “Effect of operating convection regimes (Ra_m)” section. In the next “Effect of permeability of the porous media” section, the effect of varying permeability of the porous media on the thermo-fluid structure is illustrated. The effects of different amplitudes (I) of half-sinusoidal heating on heat and flow dynamics are presented in “Influence of variation in amplitude (I) of half-sinusoidal heating” section. In “Influence of varying frequency (f) of half-sinusoidal heating” section, dynamics of the heat and fluid flow under a range of multi-frequency heating are illustrated. The effects of varying external magnetic field strength are detailed in “Impact of Hartmann number (Ha)” section. Next, “Effect of nanoparticle volume concentration (ϕ)” section demonstrates the effects of different nanoparticles volume fraction on the heat and fluid flow dynamics. The variation in local velocity, temperature, and the average Nu is illustrated in “Local velocity and temperature distributions” section. Finally, an overall heat transfer characteristics and thermal performance are reported in “Heat transfer characteristics” section for the selected effective parameters.

Effect of operating convection regimes (Ra_m)

In this section, the insights of the flow dynamics development within the enclosure along with thermal energy transportation from the heated bottom wall to the cold sidewalls are illustrated in terms of contour maps of streamlines (top row), isotherms (second row), and heatlines (third row) along with global heat transfer characteristics using average Nusselt number (below the heatline contours). The same is presented in Fig. 3 under different operating convection regimes by varying the values of Darcy–Rayleigh number ($Ra_m = 10, 10^2, 10^4$) for the fixed values of $Da = 10^{-4}$, $Ha = 30$, $f = 1$, $I = 1$, $\phi = 0.02$. As the fluid flows through

Table 3 Grid sensitivity analysis for a range of Ra_m values ($10-10^4$) at $Da = 10^{-4}$, $\varepsilon = 0.6$, $I = 1$, $f = 5$, $\phi = 0.02$, $Ha = 30$

Ra_m	Average Nu (consecutive error in %)				
	80×80	120×120	160×160	200×200	250×250
10	3.661	3.664 (0.08%)	3.665 (0.02%)	3.665 (0.01%)	3.665 (0.01%)
10^2	3.801	3.791 (0.27%)	3.785 (0.14%)	3.782 (0.09%)	3.781 (0.04%)
10^3	7.594	7.484 (1.47%)	7.433 (0.68%)	7.407 (0.36%)	7.415 (0.11%)
10^4	17.553	16.902 (3.85%)	16.561 (2.06%)	16.377 (1.12%)	16.400 (0.14%)

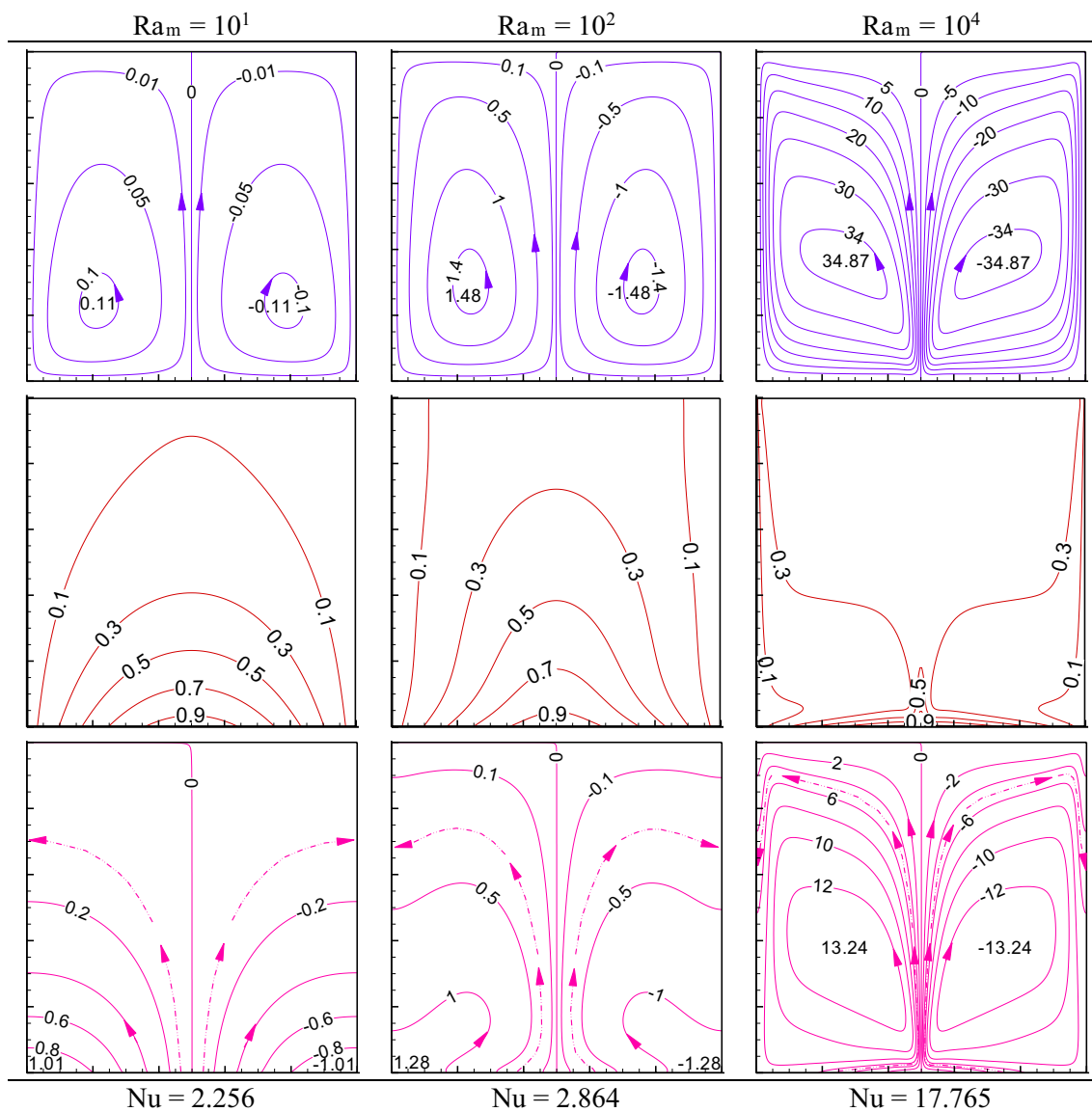


Fig. 3 (Color figure online) Effect of different Darcy–Rayleigh numbers (Ra_m) on the contour maps of streamlines (first row), isotherms (second row), and heatlines (third row) at $Da=10^{-4}$, $Ha=30$, $f=1$, $I=1$, $\phi=0.02$. The intervals for the contours are taken as 0.2 for iso-

therms; 0.05 (first column), 0.5 (second column), 5 (third column) for streamlines; 0.2 (first column), 0.5 (second column), 2 (third column) for heatlines

the porous layers, it creates resistance to flow. Thus, it is extremely pertinent to analyze the thermo-fluid behavior through the porous media using the dimensionless number of modified Rayleigh number or Darcy–Rayleigh number ($Ra_m = Ra \times Da$), which is defined in Eq. (9b).

From Fig. 3, it is observed that at a lower value of $Ra_m = 10$ (first column), the fluid layer near the heated bottom wall rises upward through the middle vertical region of the cavity due to the variation in fluid density. As the top wall is thermally insulated, upward fluid flow is obstructed by the top wall and then moved toward the sidewalls, where hot fluid rejects heat, and thereafter, the fluid is cooled and

descends down along the sidewalls. Cold fluid further takes heat from the heated bottom wall. Thus, it is found the formation of two flow vortices, which effectively occupy the entire enclosure. These vortices distribute symmetrically about the mid-vertical plane of the enclosure; one vortex (at the left part) is rotating in anticlockwise (CCW) direction (marked with a positive sign) and another vortex (at the right part) is rotating in clockwise (CW) direction (marked with negative sign). Corresponding temperature distribution patterns can be visualized from the isotherm contour maps (second row). As the cavity fluid is heated at the bottom following half-sinusoidal nonuniform heating, the

isotherm contours adjacent to the heated wall designate the peak temperature about the middle region of the enclosure and thereafter widen over the entire enclosure. For a better understanding of the heat flow dynamics within the enclosure, the Bejan's heatline contour maps are illustrated in the third row of Fig. 3. The heatlines contours originate from the heated bottom wall and are connected in between the bottom heated wall and heat sinks located at the sidewalls, and it is marked with the arrowhead. It indicates a pathway for the fixed quantity of energy transportation. Due to the half-sinusoidal heating, the heat energy is transferred through a tapered corridor (from the bottom wall to the sidewalls) about the mid-vertical planes. Thereafter, the energy flow passage widens and expands to a maximum area near to the entire sidewalls of the enclosure.

As Ra_m increases from 10 to 10^2 (second column) and 10^4 (third column), the fluid circulation strengths increase significantly and the centers of the flow vortices shift upward. It implies increment in the corresponding fluid Rayleigh numbers (Ra) from 10^5 to 10^8 . In this context, it is pertinent that as the value of Ra_m increases the convection mode of heat transfer dominates over conduction and it becomes stronger at a higher value of Ra_m . As a result, weaker fluid circulation and lower heat transportation are observed at lower Ra_m . At the higher value of Ra_m , the strength of the fluid circulation increases substantially, which is reflected by the changes in the intensity of the maximum value of streamfunction ($|\psi|_{\max}$). The higher fluid velocity is attributed due to the increase in the temperature gradient as well as an increase in the inertial force over the viscous force; it results in enhanced thermal convection. Associated temperature distribution shows the crowded lines nearer to the heated bottom wall, which is further deformed and becomes parallel to the cold sidewalls. Such distribution of the isotherms shows a significant reduction in the thermal boundary layer thickness at the heated wall and cooled walls. This fact implies the increase in heat transfer at higher Ra_m . This is also evident from the heatline contour maps as the intensity of heatlines increases, and the maximum value of heatfunction II_{\max} also increases significantly. From the heatline contour maps, one interesting observation can be found as the convective heat transfer increases at higher Ra_m , the distribution of heatlines indicates higher magnitude of energy at the central point of the bottom wall. Thereafter, the heat energy flows through a narrow passage and then spreads over the entire sidewalls. As a result, areas beyond the energy flow pathway are filled with energy flow circulation cells similar to the streamline contour maps. The formation of such energy circulation cells is observed for $Ra_m \geq 10^2$. As Ra_m increases from 10 to 10^4 , the width of the heat energy flow passage becomes narrower and the convective heat flux becomes stronger. Thus, the size of the inactive energy flow circulation cells increases. The magnitude of the enhanced convective heat transfer

characteristics can be realized from the increasing values of average Nu at the heated bottom wall (as mentioned below the heatline contours).

Effect of permeability of the porous media

In order to understand the influence of the permeability parameter of the porous medium on the thermo-fluid phenomena, the variation in dimensionless Darcy number (Da) is analyzed and illustrated in Fig. 4 for three different Da values (10^{-5} , 10^{-3} , 10^{-1}) for the fixed values of $Ra_m = 10^3$, $f = 1$, $I = 1$, $Ha = 30$, $\phi = 0.02$. In this case, $Ra_m (= Ra \times Da)$ is kept at a fixed value; as a result, the fluid-based Ra decreases with the increasing Da . Figure 4 clearly demonstrates the symmetrical distribution of flow as well as temperature within the enclosure. Generally, the fluid flow faces relatively lower resistance, when Da is increasing (as likely from the reduced permeability of the porous matrix). This leads to an increase in the fluid velocity, which in turn leads to higher heat transfer rates from the heated wall to the cold walls. However, when the fluid-flow structures and the temperature pattern of different Da values (10^{-5} , 10^{-3} and 10^{-1}) are compared, it shows an unusual pattern. As the fluid circulation strength ($|\psi|_{\max}$) becomes weaker, the maximum value of heatfunction (II_{\max}) decreases significantly; the thicker thermal boundary layer thickness is noted along the heated wall. This happens so at the fixed value of Ra_m , the fluid-based Rayleigh number decreases with increasing Da . This results in weaker circulation even at higher Da value ($= 10^{-1}$). As the fluid velocity is less, it causes very lesser penetration of the flow through the porous media, resulting in a lower heat transfer rate, which is reflected by the average Nu value.

Influence of variation in amplitude (I) of half-sinusoidal heating

The flow physics, as well as the thermal behavior within the considered geometry, is critically governed by the thermal condition of the heat source. To illustrate this, the effect of varying dimensionless amplitude $I = 0.3$, 0.5 , and 0.7 (of temperature) on the heat flow dynamics is investigated and consequent results are presented in Figs. 5 and 6, respectively, keeping fixed values at $f = 1$, $Ra_m = 10^3$, $Da = 10^{-4}$, $Ha = 30$, $f = 1$, $\phi = 0.02$. Figure 5 depicts that when the amplitude I is lower ($= 0.3$), the temperature on the bottom wall is also lower ($\theta \approx 0.3$ at the middle point of the bottom wall). Corresponding flow fields indicate weaker fluid circulation and heat energy transportation. When the amplitude I increases to 0.5 , the temperatures at the central point of the bottom wall become $\theta \approx 0.5$, and at the farthest ends it decreases (following half-sinusoidal temperature profile). As the temperature gradient increases, the heat transfer rate also increases significantly as reflected by the average Nu

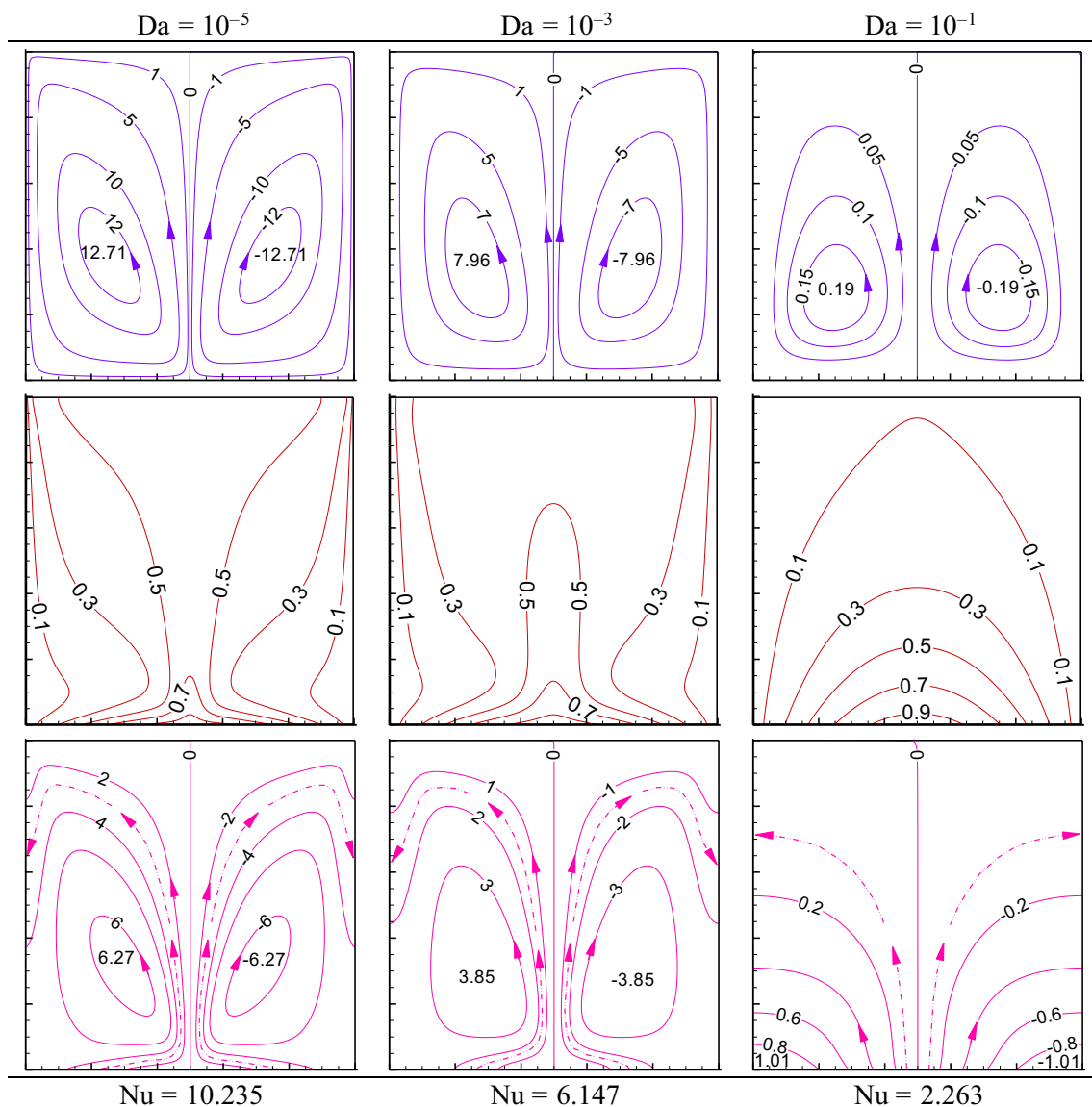


Fig. 4 (Color figure online) Effect of different Darcy numbers (Da) of the porous media on the contour maps of streamlines (first row), isotherms (second row), and heatlines (third row) at $Ra_m = 10^3$, $Ha = 30$, $f = 1$, $I = 1$, $\phi = 0.02$. The intervals for the contours are taken as 0.2

for isotherms; 5 (first and second columns), 0.05 (third column) for streamlines; 2 (first column), 1 (second column), 0.2 (third column) for heatlines

value. Further increasing the amplitude to $I = 0.7$, the above observations are amplified markedly. The maximum values of $|\psi|_{\max}$ and Π_{\max} increase noticeably, and heat transfer magnitude increases monotonously.

For an in-depth understanding of the transport phenomena over the heated bottom wall under the varying amplitude I , Fig. 6 illustrates the blow-up view (for the lower portion of the enclosure) of the changes in the isotherms superimposed velocity vectors for $I = 0.3, 0.5$, and 1 at two different $Ra_m = 10^3$ (Fig. 6a) and 10^4 (Fig. 6b), respectively, for the fixed values of $Da = 10^{-4}$, $Ha = 30$, $f = 1$, $\phi = 0.02$. From Fig. 6a, it is observed that as I increases from 0.3

to 0.5 and 1, the temperature distribution along the bottom wall changes significantly. Furthermore, the peak in the temperature also modifies. The phenomena of velocity as well as thermal boundary layers can be visualized easily close to the bottom wall. From both sides, the cold fluids move downwards along the sidewalls and take a sharp turn ($\sim 90^\circ$) as it faces temperature near the bottom wall. Thereafter, it becomes an almost parallel pattern with the bottom wall and finally climbs upward and forms a central plume. The isotherm lines near to the bottom wall indicate the growth of the increasing boundary layer thickness at both halves of the enclosure. Of course, such a scenario of the boundary layer

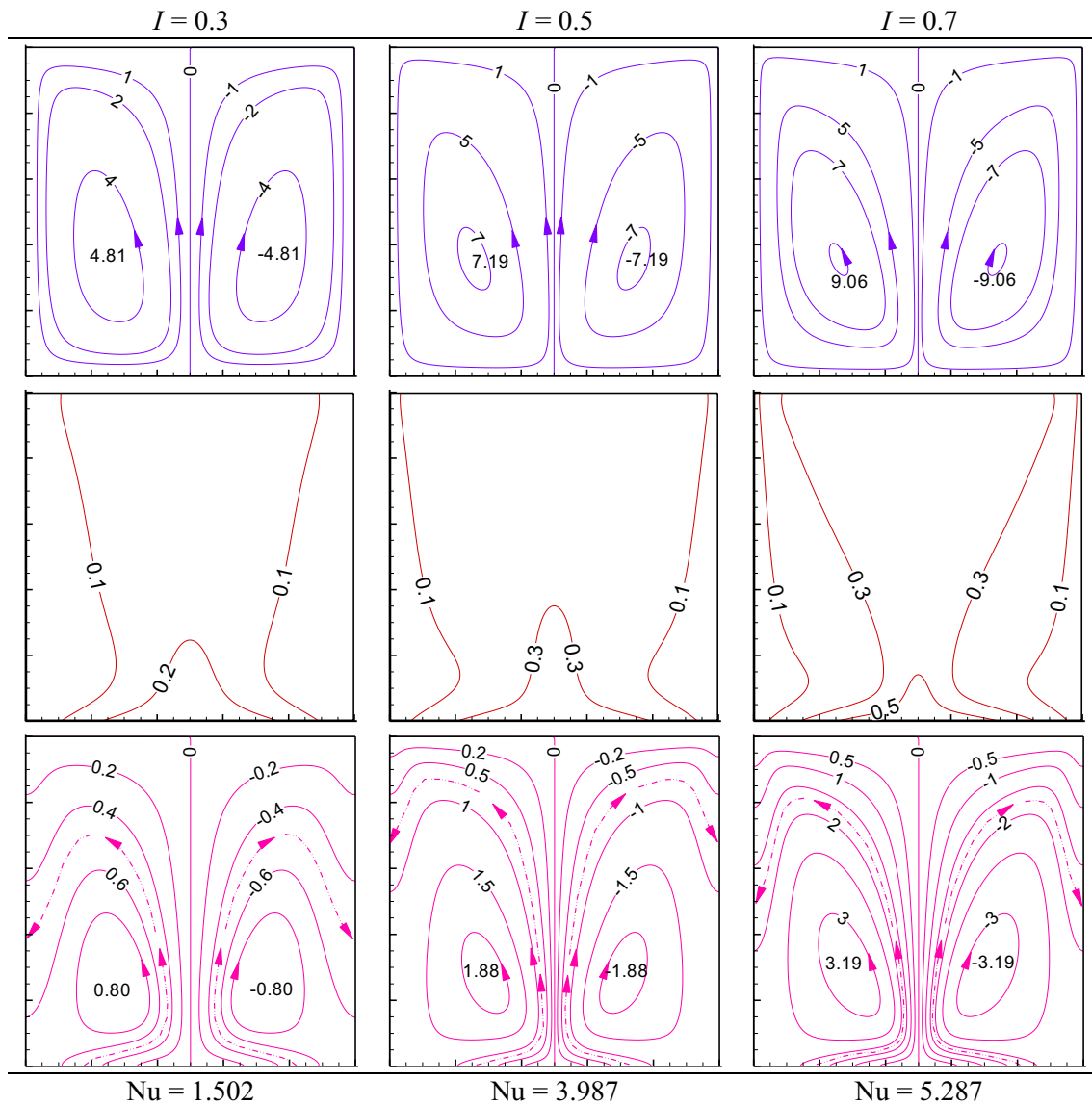


Fig. 5 (Color figure online) Effect of different amplitudes of half-sinusoidal heating (I) on the contour maps of streamlines (first row), isotherms (second row), and heatlines (third row) at $Ra_m = 10^3$, $Da = 10^{-4}$, $Ha = 30$, $f = 1$, $\phi = 0.02$. The intervals for the contours are

taken as 0.1 for isotherms; 1 (first column), 5 (second and third columns) for streamlines; 0.2 (first column), 0.5 (second and third columns) for heatlines

and fluid flow pattern modifies severely at higher amplitude $I = 1$ and higher value of Ra_m as shown in Fig. 6b. As the bottom wall is heated nonuniformly (following half-sinusoidal temperature condition), such unusual boundary layers grow monotonously (compared to uniform heating condition, not shown here) and it appears in a periodic manner. Corresponding velocity vectors clearly indicate the convective velocity (comparing the same reference vector), and its magnitude is markedly higher at $Ra_m = 10^4$ compared to $Ra_m = 10^3$. At the higher value of Ra_m , the fluid circulation is higher due to higher thermal energy transportation and it is

stronger at $I = 1$, which is reflected by the densely distributed velocity vectors.

Influence of varying frequency (f) of half-sinusoidal heating

Further to the aforementioned analysis, the impact of variation in frequency f of nonuniform heating (following half-sinusoidal temperature profile) on the dynamics of thermo-fluid flow is investigated and illustrated in Fig. 7 for three different frequencies $f = 3, 5$, and 10 keeping other parameters fixed at $Ra_m = 10^3$, $Da = 10^{-4}$, $I = 1$, $Ha = 30$, $\phi = 0.02$.

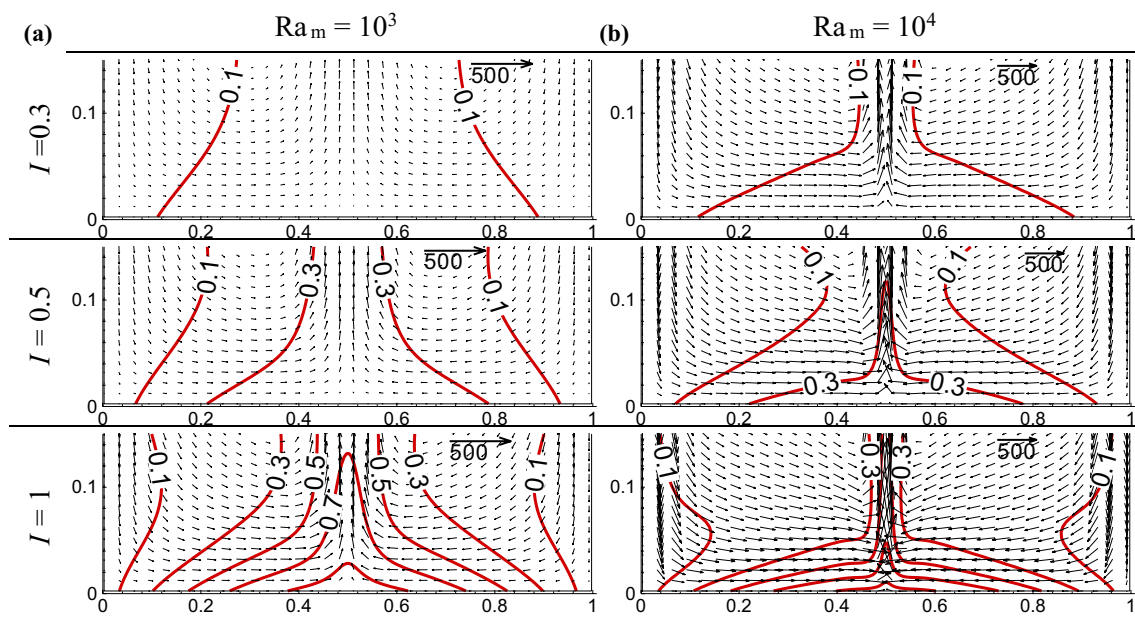


Fig. 6 (Color figure online) Thermo-fluid flow phenomena near boundary of the bottom heated wall in terms of the velocity vectors and isotherms under multi-frequency half-sinusoidal heating for **a** $Ra_m = 10^3$ and **b** $Ra_m = 10^4$ at $Da = 10^{-4}$, $Ha = 30$, $f = 1$, $\phi = 0.02$

Recalling earlier findings of overall flow structure (twin circulations), temperature distribution, Fig. 6 exhibits similar dynamics except for the bottom region (near to the heated wall) of the cavity and it persists for any spatial frequencies. Compared to the single frequency ($f = 1$), the strength of the fluid circulation (as denoted by $|\psi|_{\max}$) and a maximum value of heatfunction Π_{\max} decrease with the increasing frequency. Of course, near-wall thermo-fluid flow behavior becomes more sensitive and complex at higher spatial frequencies. An increase in the frequency, overall flow structure doesn't alter markedly, except the lower portion close to the heated bottom wall. It causes a modulation of both streamlines and isotherms with the change in the frequency. As the frequency increases, a number of tiny fluid circulation and energy circulation cell form, and this number is basically a function of the multi-frequency of heating. The temperature distribution (isotherms panel) of fluid nearer to the bottom wall indicates the presence of different numbers of peaks (3 peaks for $f = 3$, 5 peaks for $f = 5$, 10 peaks for $f = 10$ following the frequency of half-sinusoidal heating). Evidently, the temperature of the fluid layers close to the heated wall changes following the heating condition.

Of course, in between any two temperature peaks a fall in the fluid temperature is noticeable, which is attributed due to the intermediate cooling (where θ approaches 0 value) of hot fluid by rejecting out heat through this wall. At the higher f values, more numbers of low-temperature points are noticeable. This results in a wavy pattern in streamlines as well as heatline contours maps (as in the first and third rows, respectively). It should be mentioned here that, due to

intermediate cooling at the bottom wall, the magnitude of the overall heat transfer characteristic denoted by the average Nu (at the heated wall) decreases compared to the case of a single frequency ($f = 1$) of the half-sinusoidal heating. The maximum values of $|\psi|_{\max}$ and Π_{\max} decrease marginally.

For a better understanding of the multi-frequency of half-sinusoidal heating effect on the heat flow dynamics, the blow-up view (for the lower portion of the enclosure) of the isotherms superimposed velocity vectors is analyzed for three different frequencies $f = 3, 5$, and 10 and is illustrated in Fig. 8a, b at two different $Ra_m = 10^3$ and 10^4 , respectively, keeping other parameter fixed at $I = 1$, $Ha = 30$, $\phi = 0.02$. As f increases from 1 (as shown in Fig. 6a, b—bottom row) to 3, 5, and 10, the temperature distribution along the bottom wall changes markedly. As the frequency f increases, the isotherm lines indicate the presence of multiple peaks over the entire heated wall and there exist velocity and thermal boundary layers stretched over the bottom wall. These numbers of peaks in isotherms (1 peak for $f = 1$, 3 peaks for $f = 3$, 5 peaks for $f = 5$ and 10 peaks for $f = 10$) are also a function of the half-sinusoidal frequency. Height in the peaks is also modulated by the frequency variation; the higher frequency causes a decrease in height of the peaks (although the number of peaks increases). From both sides, the downward-moving cold fluid takes a sharp turn ($> 90^\circ$) as it faces temperature peaks near the bottom corners. Thereafter, it takes a wavy pattern and finally climbs upward and forms a central plume. The isotherm line near to the bottom wall indicates the growth of the wavy boundary layer at both halves of the enclosure. The formation of such undulation

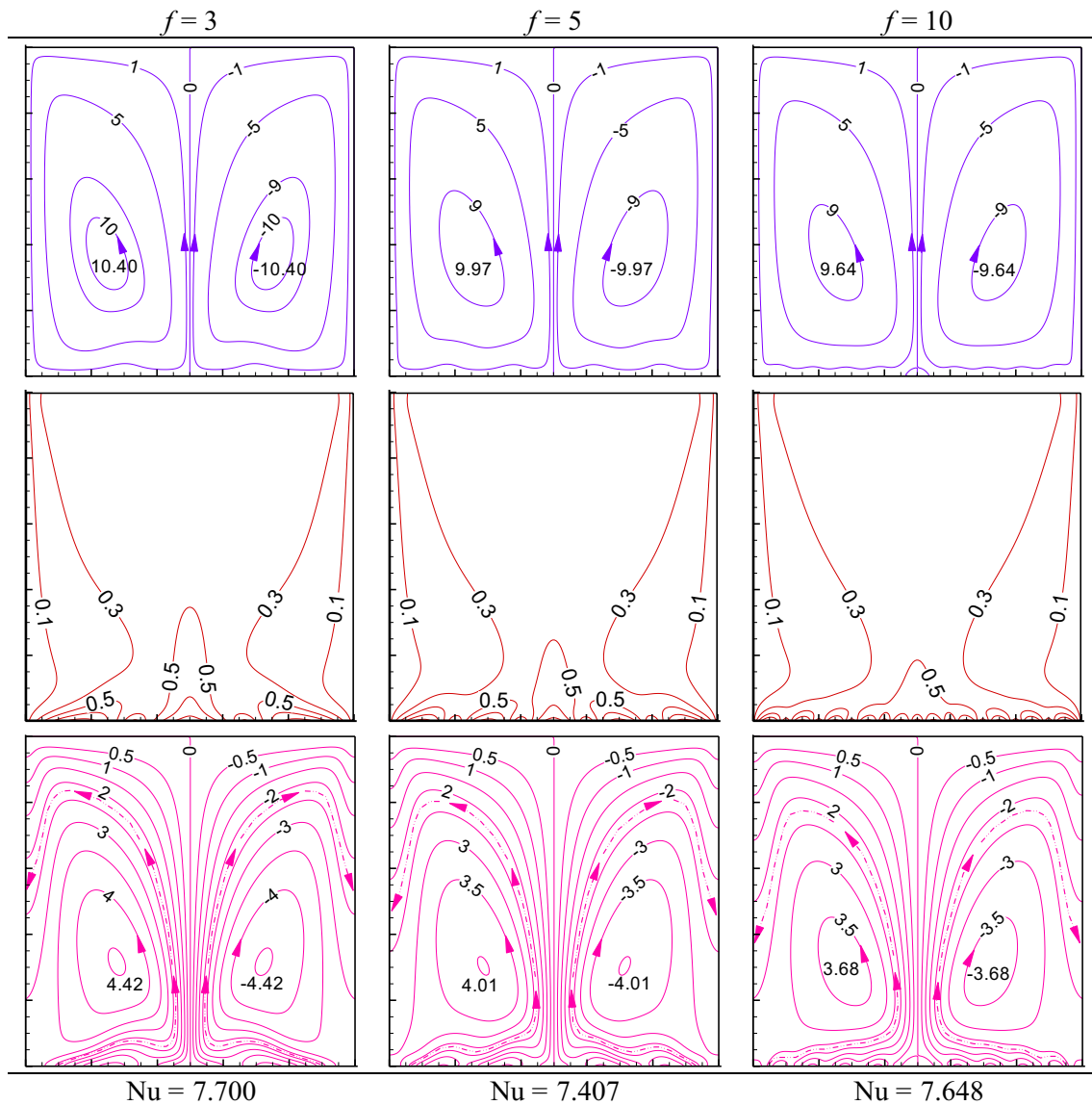


Fig. 7 (Color figure online) Effect of frequency of half-sinusoidal heating (f) on the contour maps of streamlines (first row), isotherms (second row), and heatlines (third row) at $Ra_m=10^3$, $Da=10^{-4}$,

$Ha=30$, $I=1$, $\phi=0.02$. The intervals for the contours are taken as 0.1 for isotherms, 5 for streamlines, 2 for heatlines

is more complex till $f=5$, beyond which the undulation decreases as the isotherm peak height decreases. Such circumstances of the boundary layers and the fluid flow pattern modify severely at the higher Ra_m as shown in Fig. 8b. Interestingly, as the bottom wall is heated nonuniformly (following half-sinusoidal temperature condition), there exists a lower temperature at some points (as θ approaching 0 value). This results in an intermediate cooling effect of the hot fluid through the same bottom wall. This results in the formation of the wavy boundary layers, which is also supported by the velocity vector distribution. Such a usual boundary layer grows monotonously (compared to the case of the uniform heating condition, not shown here), and it

appears in a periodic manner. Comparing the same reference vector length, the velocity vector distribution clearly indicates the convective velocity, which increases significantly at $Ra_m=10^4$ compared to that of $Ra_m=10^3$. At the higher value of Ra_m , densely distributed velocity vectors indicate a higher strength of fluid circulation due to higher thermal energy transportation.

Impact of Hartmann number (Ha)

The impact of the externally applied magnetic field, denoted by the dimensionless Hartmann number (Ha), on the thermo-fluid flow is investigated and presented in Fig. 9 for $Ha=0$

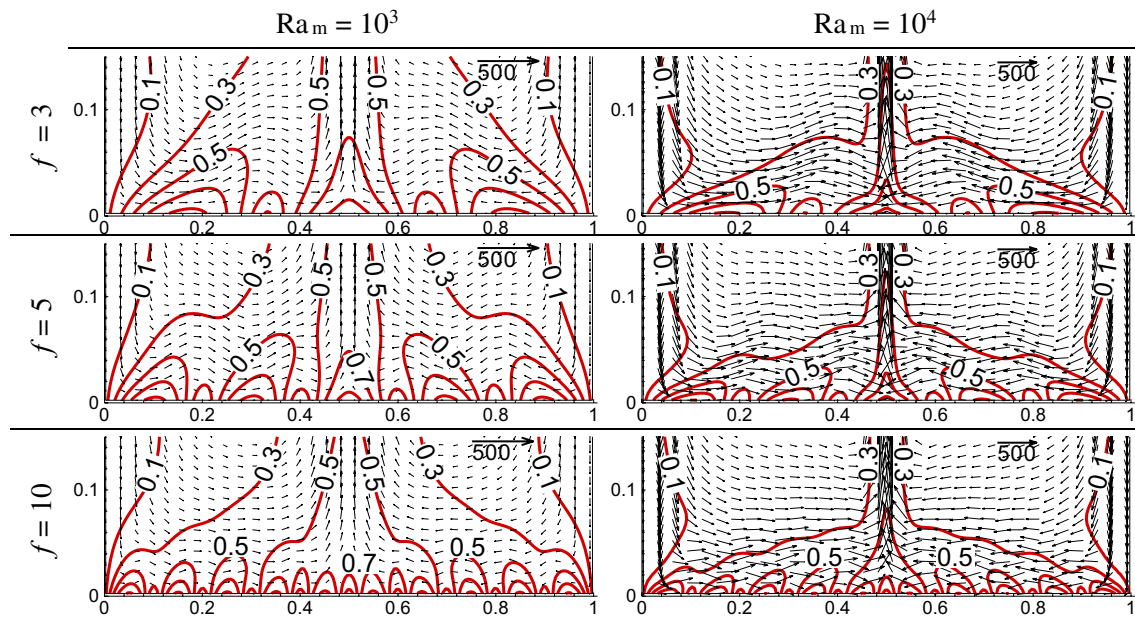


Fig. 8 (Color figure online) Thermo-fluid flow phenomena near boundary of the bottom heated wall in terms of the velocity vectors and isotherms under multi-frequency half-sinusoidal heating for **a** $Ra_m = 10^3$, and **b** $Ra_m = 10^4$ at $Da = 10^{-4}$, $Ha = 30$, $I = 1$, $\phi = 0.02$

(no magnetic field), 10, and 50 considering other parameters fixed as $Ra_m = 10^3$, $Da = 10^{-4}$, $f = 1$, $I = 1$, $\phi = 0.02$. For the understanding of in-depth flow physics under different magnetic fields, the no magnetic field case is simulated first and presented in the first column of Fig. 9. In general, there is no alteration in the fluid flow as well as energy transportation. However, without a magnetic field, the heat transfer is dominated by the thermal convection only. Of course, the presence of a magnetic field reduces the fluid velocity and such retardation is higher at higher Ha value. The reason behind such a reduction in the velocity can be easily understood. From the momentum Eq. (7), it is apparent that the presence of negative source terms (containing the Ha parameter) causes a decrease in the vertical velocity component as Ha increases. Hence, the magnetic force term counteracts the positive consequence of the buoyancy force. This results in a further reduction in the fluid velocity, which also puts some impacts on the energy Eq. (8). As a result, thermal energy transportation reduces with increasing Ha values. As the Ha value changes from 0 to 10 and then 50, the negative impact on the fluid flow, temperature distribution, and heatline contours is clearly noticeable from the magnitude of $|\psi|_{\max}$ and Π_{\max} . The associated heat transfer rate also decreases as reflected by the Nu values.

Effect of nanoparticle volume concentration (ϕ)

Figure 10 depicts the effects of the addition of Cu–Al₂O₃ hybrid nanoparticles in the pure fluid (water) on the thermo-fluid flow structure under multi-frequency half-sinusoidal

heating conditions at $Ra_m = 10^3$, $I = 1$, $f = 1$, $Ha = 30$. For the comparison with no nanoparticles addition situation, the case of pure fluid ($\phi = 0$) is simulated first under similar thermal boundary condition and presented in the first column of Fig. 10; thereafter, the case of two different volume concentrations of Cu–Al₂O₃ hybrid nanoparticles ($\phi = 0.001$ and 0.03) is illustrated in the second and third columns, respectively. All the streamlines, isotherms, and heatline contours show the symmetrical distribution, and there is no such significant deviation in the contour maps for a different fraction of hybrid nanofluid volume concentrations. On the other hand, the addition of 0.001 Cu–Al₂O₃ hybrid nanoparticles in the pure water leads to a considerable increment in the fluid velocity compared to base fluid ($\phi = 0$) as denoted by the magnitude of $|\psi|_{\max}$. This is attributed to the effects of the enhanced inertia force compared to the viscous force, as the effective thermal conductivity increases significantly with the addition of hybrid nanoparticles [36, 81]. As a result, the overall heat transfer rate increases compared to the case of pure water, which is reflected by the average Nu value. However, further augmentation of the hybrid nanoparticles concentration to 0.03 shows a decreasing trend of fluid velocity, heat energy transportation, and associated heat transfer, which is reflected by and ψ_{\max} , Π_{\max} and the average Nu values, respectively. This is attributed due to the fact that by the addition of different combinations of nanoparticles into the base fluid, the effective dynamic viscosity increases. A higher concentration of hybrid nanoparticles causes more resistance to the fluid velocity through the increased shear stresses. Thus, the viscous force dominates over the inertia

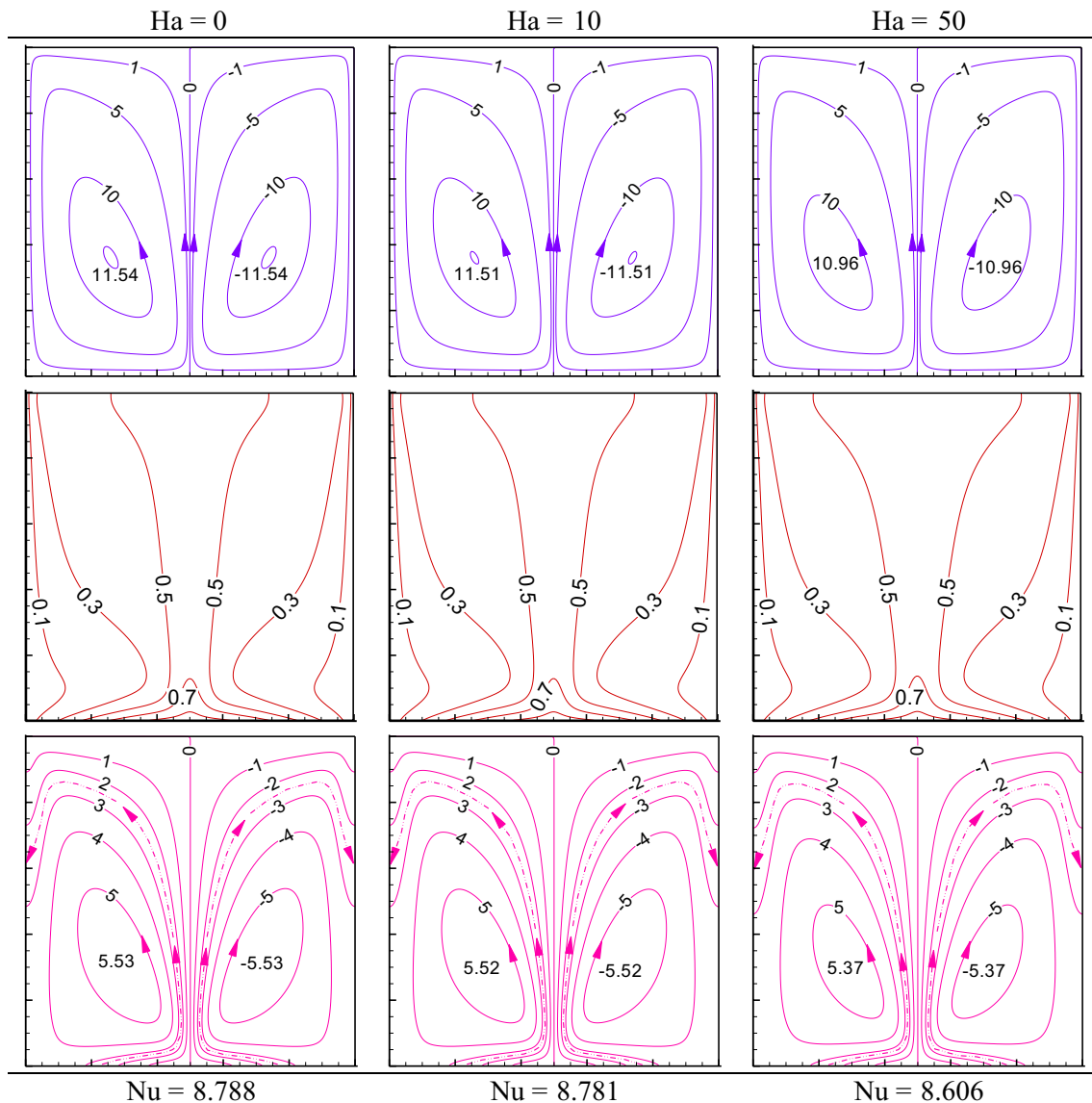


Fig. 9 (Color figure online) Effect of magnetic field strength in terms of Hartmann number (Ha) on the contour maps of streamlines (first row), isotherms (second row), and heatlines (third row) at $Ra_m = 10^3$,

$Da = 10^{-4}$, $f = 1$, $I = 1$, $\phi = 0.02$. The intervals for the contours are taken as 0.1 for isotherms, 5 for streamlines, 1 for heatlines

force. This leads to a reduction in fluid motion as well as heat energy transportation. As a result, the advection mechanism reduces and the associated overall heat transfer rate reduces (reflected by the average Nu values). Similar findings have already been documented in refs. [36, 67–69, 81].

Local velocity and temperature distributions

For the completeness of the analysis and in-depth understanding of the thermo-flow physics, dimensionless local distribution of a vertical velocity component (V) and temperature (θ) at the mid-vertical plane ($Y = 0.5$) is analyzed and presented in Fig. 11 under half-sinusoidal heating

condition. The effect of Ra_m and Da (and also frequency and amplitude of half-sinusoidal heating) on the profile plots of vertical velocity and temperature is understandably not uniform across the width of the enclosure as shown in Fig. 11. It happens so as the governing momentum equations are nonlinear and coupled to temperature and pressure, and also involving the presence of different forces, namely buoyant force, magnetic force, pressure force, and Darcy and Forchheimer contributing force terms. The velocity and temperature become the function of the coordinate position (X, Y) and all the parameters (Ra_m, Da, Ha, f, I, ϕ). All the governing equations are solved by applying the specific boundary conditions for different walls of the enclosure.

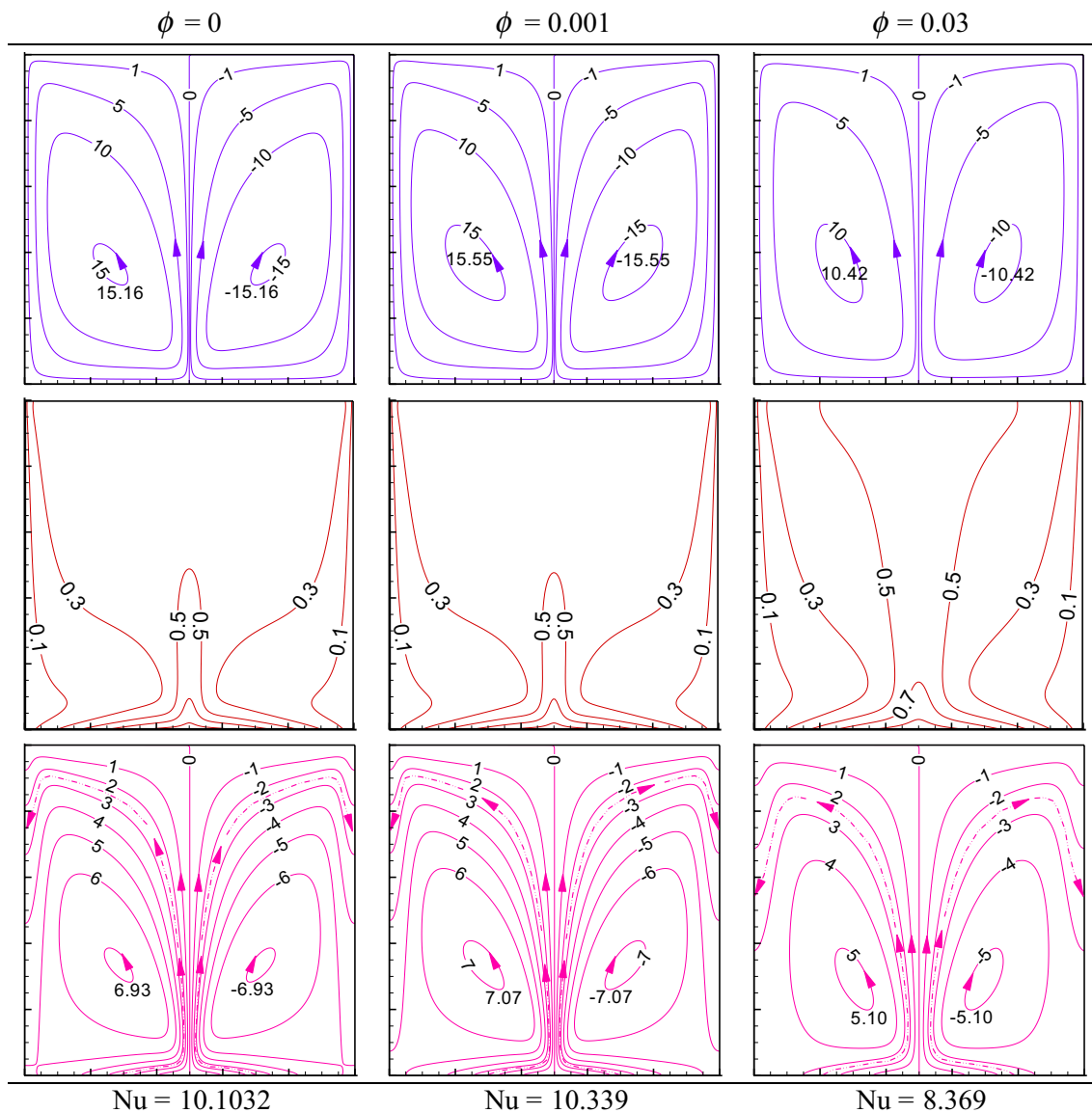


Fig. 10 (Color figure online) Effect of Cu–Al₂O₃ hybrid nanoparticle concentration (ϕ) on the contour maps of streamlines (first row), isotherms (second row), and heatlines (third row) at $Ra_m = 10^3$,

$Da = 10^{-4}$, $Ha = 30$, $f = 1$, $I = 1$. The intervals for the contours are taken as 0.2 for isotherms, 5 for streamlines, 1 for heatlines

The distribution of the variables (U , V , P and θ) within the computing domain depends upon the governing equations, constitutive relations, and the applied boundary conditions. Thus, the profiles of V and θ become nonuniform for any values of Ra_m and Da . Particularly due to the fluid viscosity, the formation of boundary layers, bottom heating, and side cooling, the profiles become nonuniform across the width of the enclosure.

The variation in the V velocities and θ for different frequencies $f = 1, 3, 5$, and 10 is presented in Fig. 11a for the fixed values of $Ra_m = 10^3$, $Da = 10^{-4}$, $I = 1$, $Ha = 30$, $\phi = 0.02$. Figure 11a depicts a high positive peak at the center (about $X = 0.5$) and two negative peaks toward both

ends of the X -axis. This is attributed due to the formation of the thermal plume and two counterrotating flow vortices inside the enclosure. As the frequency increases, the peak velocity decreases marginally which is also evident from contour maps (as shown in Fig. 7). Corresponding nondimensional mid-plane temperature distribution supports the above findings, as θ is higher at the central point and θ approached to zero toward the sidewalls ($X = 0$ and 1) of the enclosure. With the increasing f , the peak value of θ decreases marginally and this is due to the reduction in thermal convection.

Figure 11b shows the effects of the variation in V velocity and θ for different values of dimensionless amplitude

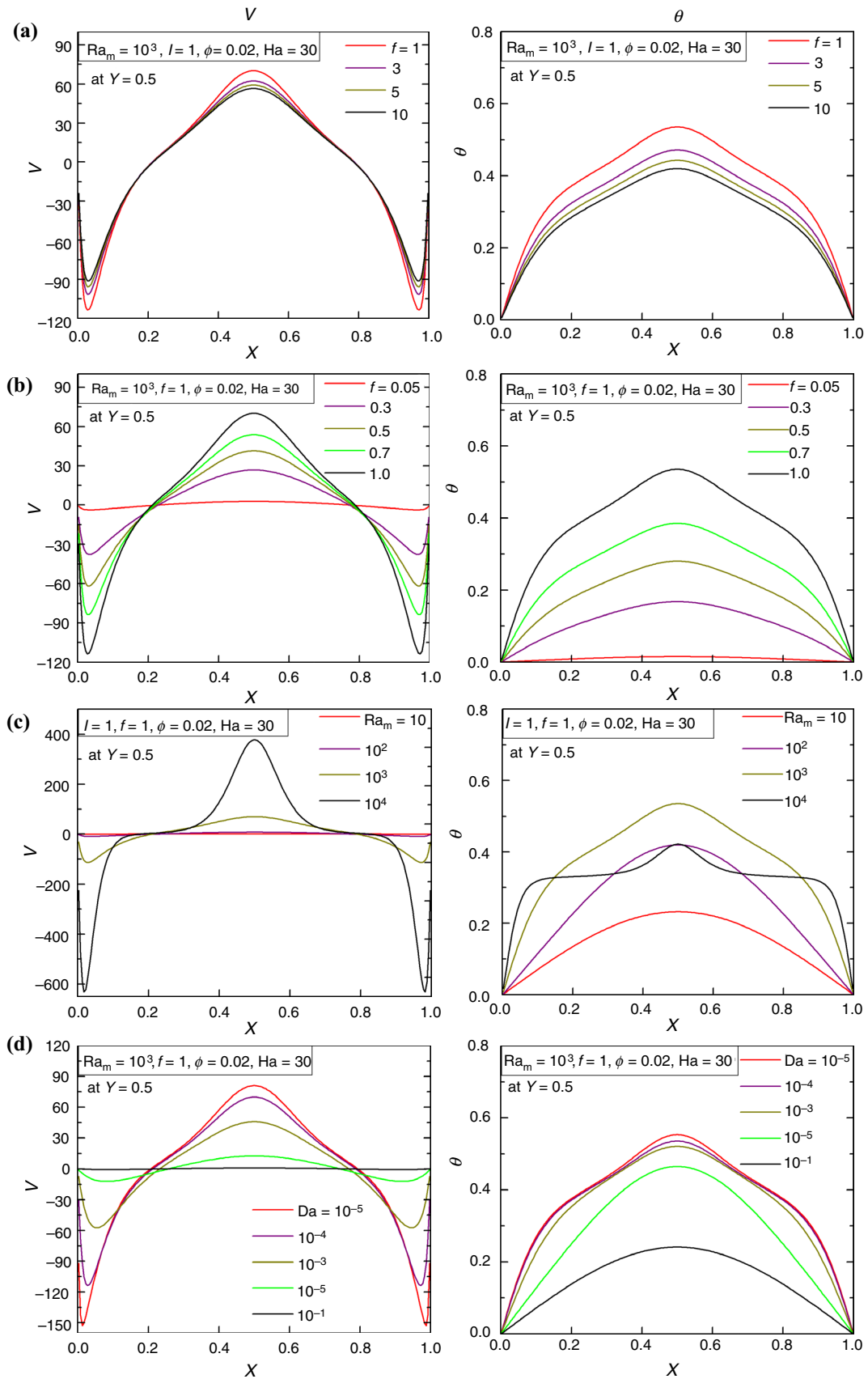


Fig. 11 (Color figure online) Mid-plane profiles of vertical velocity component (V) and temperature (θ) for varying **a** frequency (f), **b** amplitude (I) of half-sinusoidal heating (temperature), **c** Darcy–Rayleigh number (Ra_m), **d** Darcy number (Da), keeping other parameters fixed at $\phi=0.02$, $Ha=30$

$I=0.05, 0.3, 0.5, 0.7$, and 1 for the fixed values of $Ra_m=10^3$, $Da=10^{-4}$, $f=1$, $Ha=30$, $\phi=0.02$. The V velocity and θ plot indicates a wider range of variation in its dimensionless magnitudes. As the temperature of the fluid layers close to the bottom wall modifies drastically following the imposed heating condition—the local variation as well as mid-plane velocity and temperature along the X direction is affected severely and it modulates the dynamics of fluid flow and heat transfer. At a very low amplitude ($I=0.05$), the temperature gradient is very low and it results in a very weaker thermal plume as well as weaker temperature. However, thermal convection increases substantially at every step increment of the amplitude. Associated heat transfer also increases markedly.

Figure 11c shows the effects of varying $Ra_m=10, 10^2, 10^3, 10^4$ on the V velocity and θ for the fixed the values of $Da=10^{-4}$, $f=1$, $I=1$, $Ha=30$, $\phi=0.02$. At a lower value of Ra_m , the thermal conduction (mode) drives the fluid flow as well as temperature distribution. Corresponding fluid motion is insignificantly weak. Of course, for $Ra_m>10$, thermal convection mode dominates over the thermal conduction, resulting in the higher convective heat transfer and a significant rise in the V velocity. At every step of rise in Ra_m , the inclination of θ curve indicates marked changes. On the other hand, the permeability of the porous medium has a significant role in the thermal behavior of the system. Figure 11d depicts the effect of different $Da=10^{-5}, 10^{-4}, 10^{-3}, 10^{-2}$ and 10^{-1} on the V velocity and θ distribution for the fixed values of $Ra_m=10^3$, $Da=10^{-4}$, $f=1$, $I=1$, $Ha=30$, $\phi=0.02$. The V velocity and θ profile shows opposite trends (as expected from the usual notion) with increasing Da . With the increase in Da , the fluid velocity is supposed to be increasing—as the fluid flow faces less resistance. However, in the present study, $Ra_m (=Ra \times Da)$ is kept constant at 10^3 for analyzing the effect of permeability of the porous medium by varying Da . As a result, the fluid-based Ra decreases with increasing Da . It causes a decrease in the fluid velocity and in turn temperature, which reduces the heat transfer from the heated wall. At a higher $Da (=10^{-1})$, the local variation in mid-plane velocity and temperature along the X direction is affected severely. At this Da value, the associated fluid Ra becomes very low ($=10^4$), and the conduction mode of heat transfer controls the heat transfer, resulting in very low Nu value.

It is very pertinent to scrutinize the temperature profile along the heated wall under selected parameters for the half-sinusoidal nonuniform heating condition, and it is presented in Fig. 12a, b. Figure 12a depicts the variation in the local

temperature θ along the X direction over the entire source length at $Ra_m=10^3$, $Da=10^{-4}$, $I=1$, $Ha=30$, $\phi=0.02$ under different frequency values ($f=1, 3, 5$, and 10). At the single frequency ($f=1$), the temperature at the center of the bottom wall is maximum and approaches zero at both ends (due to the presence of cold sidewalls) following the imposed half-sinusoidal temperature profile. Accordingly, the near-node fluid temperature changes (this is obvious in the steady-state situation). As the frequency increases from 1 to 3 , there appear three numbers of temperature peaks at equidistance along the length X . In addition to both ends of low-temperature points ($\theta \approx 0$), a depression in the temperature ($\theta > 0$) appears at the two more points as shown in the figure. This is attributed due to the imposed temperature condition. As a result, the slope of the temperature curve becomes sharper. Such kind of oscillation of the temperature profile is periodic in nature, and the oscillation is more as frequency f is increased to 5 or 10 . As a result, more temperature depression points are noted. This results in loss of the heat of the cavity fluid through this bottom wall, leading to the lowering of thermal convection in the enclosure. Earlier findings (as shown in Figs. 7, 8) also support the above facts. On the other hand, Fig. 12b shows symmetrical temperature profiles at the bottom wall for the varying amplitude ($I=0.05, 0.3, 0.5, 0.7$, and 1) of the half-sinusoidal heating at $Ra_m=10^3$, $Da=10^{-4}$, $f=1$, $Ha=30$, $\phi=0.02$. As I increases from 0.05 , the temperature profile along the bottom wall X changes markedly. Thus, the near-wall fluid temperature modifies noticeably. As the frequency $f=1$, the dimensionless temperature (θ) peak remains at the central point of the bottom wall. The peak temperature increases markedly with the increasing I . This results in higher thermal convection, which is also supported in the earlier findings as shown in Figs. 5 and 6.

Heat transfer characteristics

Local heat transfer rate: local Nusselt number

Further to the aforementioned analysis, it is pertinent to investigate the distribution of the local Nusselt numbers at the heated bottom wall. Following the half-sinusoidal heating (temperature) condition, the variation in local Nusselt number (Nu) changes as the dimensionless local temperature (θ) changes. The variation in the local Nu under the effect of varying frequencies (f) is depicted in Fig. 13a, b for two different $Ra_m=10^4$, and $Ra_m=10^3$ for the fixed values of $Da=10^{-4}$, $I=1$, $Ha=30$, $\phi=0.02$. As observed in Fig. 12, the dimensionless local temperature (θ) oscillates along the length of the bottom wall as both the heating and cooling take place at the same wall in an alternate manner (following the frequency of half-sinusoidal heating). At both ends of the bottom wall, the temperature difference

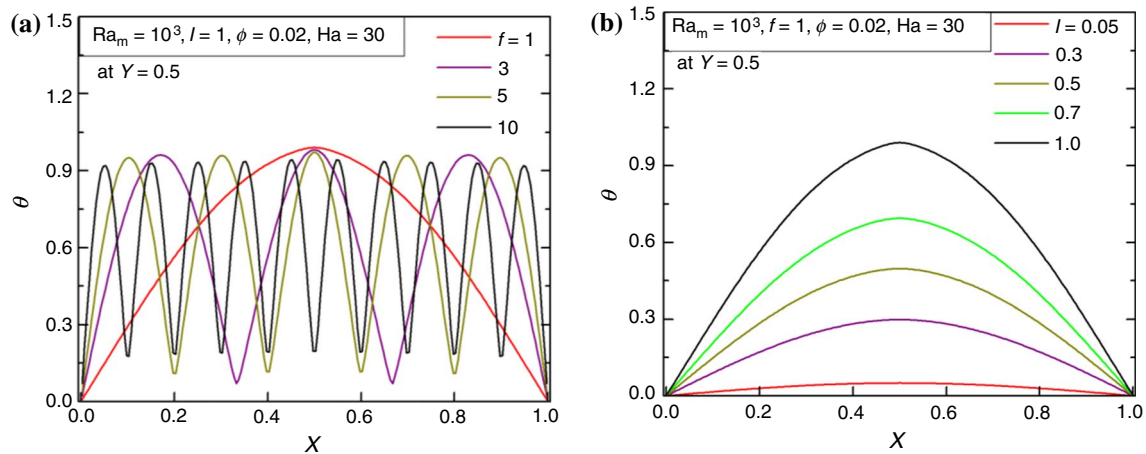


Fig. 12 (Color figure online) Variation in dimensionless local temperature (θ) along the half-sinusoidally heated bottom wall under the effect of varying, **a** frequency (f), **b** amplitude (I) at fixed values of $Ra_m = 10^3$, $\phi = 0.02$, $Ha = 30$

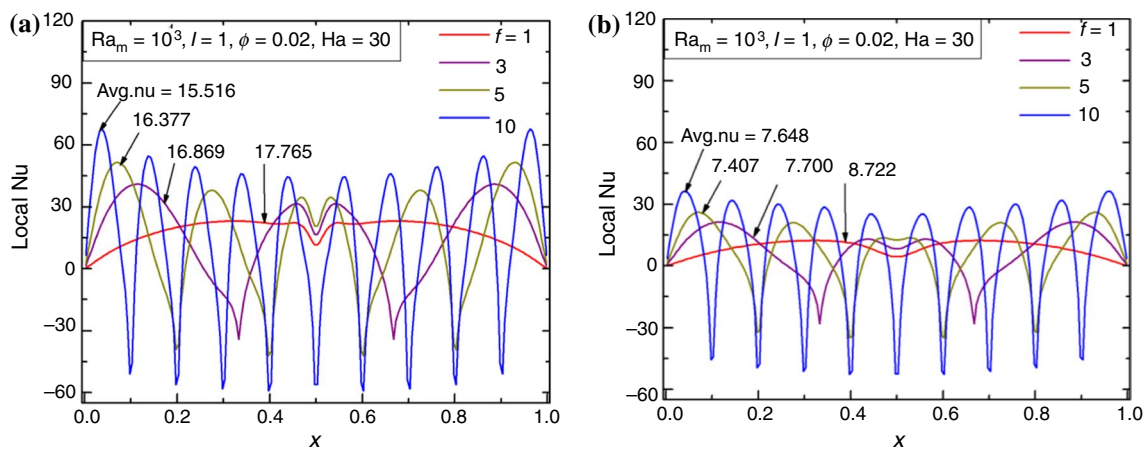


Fig. 13 (Color figure online) Variation in local Nusselt number (Nu) under the effect of varying frequency (f) for **a** $Ra_m = 10^4$, **b** $Ra_m = 10^3$ at fixed values of $Da = 10^{-4}$, $I = 1$, $\phi = 0.02$, $Ha = 30$

with the sidewalls becomes almost zero. Thus, the local Nu shows “0” value and thereafter starts increasing toward the central point. The local Nu profile reveals one interesting fact that local Nu can be positive and negative following the dimensionless temperature profile and it oscillates in a periodic manner. Increasing the frequency f from 1 to 3, 5, or 10, the local Nu severely affected due to the variation in the local temperature. Thus, the rate of local as well as average heat transfer rate decreases (as more number of depression points for temperature or intermediate cooling appears periodically). At the higher frequencies, the peak values of the local Nu (both positive and negative) are found to be consistently higher. However, the average Nu affected and it decreases. Patternwise, Fig. 13b exhibits similar nature with that of Fig. 13a except for the magnitude of local as well as average Nu , as at the lower Ra_m , the magnitude of Nu decreases.

Further to the above, the variation in local Nu under the effect of different Ra_m and Da is presented in Fig. 14a, b for the fixed values of $I = 1$, $f = 1$, $Ha = 30$, $\phi = 0.02$. In continuation with the finding of Figs. 3 and 11c, as Ra_m increases from 10 to 10^2 , convective heat transfer mode starts to dominate and becomes maximum at $Ra_m = 10^4$. As a result, the temperature gradient with the sidewalls increases. This results in higher local temperature at the heated wall as well as near-wall fluid temperature, which in turn leads to higher local Nu distribution (and higher average Nu). The slope of the local Nu curve with the cold wall decreases markedly with the increasing Ra_m . Interestingly, as Ra_m increases, the peak depression in the local Nu profile is noted about the central point of the bottom wall. This is attributed due to the fact that as the convective heat transfer becomes stronger with the increasing Ra_m , it leads to a higher local temperature as well as higher fluid circulation. As a result, cold

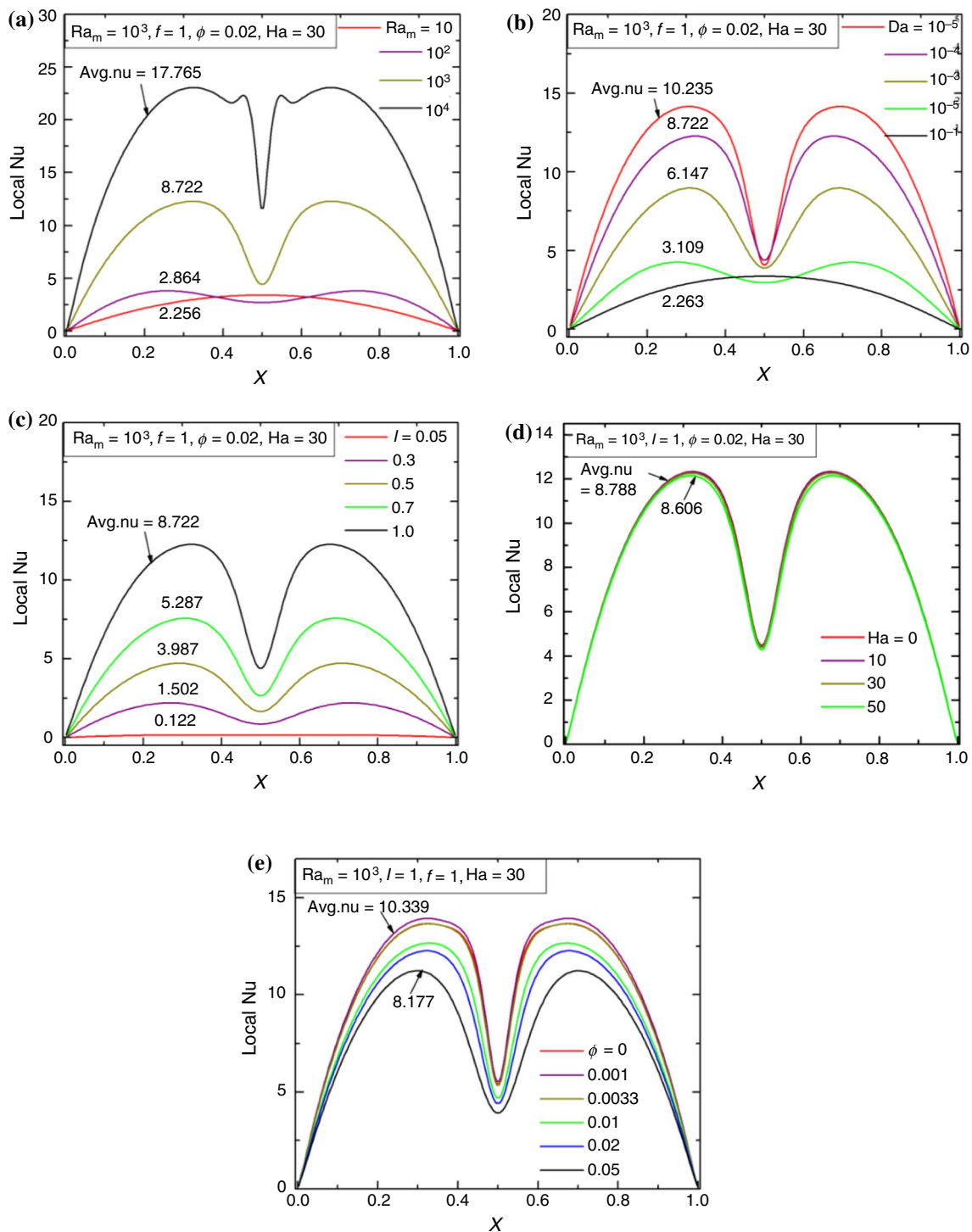


Fig. 14 (Color figure online) Variation in local Nusselt number (Nu) under the effect of varying **a** Darcy–Rayleigh number (Ra_m), **b** Darcy number (Da), **c** amplitude (l) of half-sinusoidal heating (temperature),

d Hartmann number (Ha), **e** Cu–Al₂O₃ hybrid nanoparticles volumetric concentration (ϕ) keeping a fixed value of $f=1$

fluids from both ends ($X=0, 1$) strikes the heated bottom wall and faces increasing temperature and it moves toward the center. It leads to a higher heat removal rate from the heated wall, as indicated by the increasing local Nu curve.

However, after traversing a few distances, the cold fluid temperature reaches the heated wall temperature, leading to a decrease in the temperature difference with the heated wall and reduction in horizontal fluid velocity. Furthermore, as

the fluid streams from both the ends rush toward the central plane of the enclosure ($X=0.5$) and strikes over each other, it leads to the formation of a stagnation zone over certain horizontal portions near the heated wall. It causes no more heat transfer from the heated wall. As a result, the sharp fall in the local Nu around $X=0.5$ is noted. This is an interesting finding of this case study. On the other hand, the variation in Da for the fixed values of $Ra_m = 10^3$, $I=1$, $f=1$, $Ha=30$, $\phi=0.02$ as shown in Fig. 14b depicts significant alteration in the local Nu profile as Da is increasing. Of course, as observed in Figs. 4 and 11d, lower Da corresponds to the higher fluid Ra; it results in a higher local Nu as well as higher average Nu values. The intensity of local Nu decreases significantly with increasing Da; although resistance to flow decreases, simultaneously fluid Ra decreases. Thus, the depression in the local Nu about the central point of the bottom wall decreases.

The variation in the local Nu with the varying I of half-sinusoidal heating (temperature) as shown in Fig. 14c (for $Ra_m = 10^3$, $Da = 10^{-4}$, $f=1$, $Ha=30$, $\phi=0.02$) also illustrates similar trends of local Nu distribution like Fig. 14b. However, as I increases from 0.05 to 1, the dimensionless local temperature (θ) along the heated bottom wall increases markedly (as shown in Fig. 12b). Thus, the slope of the local Nu curve with the sidewalls decreases. It leads to an increase in the local Nu as well as average Nu. Similarly, depression in the local Nu about the central point of the bottom wall increases. The variation in local Nu under different strengths of the imposed magnetic fields ($Ha=0, 10, 30$, and 50) is plotted in Fig. 14d for the fixed values of $Ra_m = 10^3$, $Da = 10^{-4}$, $f=1$, $I=1$, $\phi=0.02$. However, there is no marked change in the local Nu distribution with the increasing Ha values.

Finally, Fig. 14e depicts the variation in local Nu under different concentrations of Cu–Al₂O₃ hybrid nanoparticles (ϕ) keeping fixed values of $Ra_m = 10^3$, $Da = 10^{-4}$, $f=1$, $I=1$, $Ha=30$. The addition of Cu–Al₂O₃ hybrid nanoparticles in the base liquid increases the local Nu profile as well as average Nu up to $\phi < 0.33\%$, beyond which Nu value decreases. Such a decreasing effect of Nu is also observed in Fig. 10. Of course, the depression in the local Nu profile about the middle point of the bottom wall is persistent.

Overall heat transfer and average Nusselt number

Now the overall thermal performances of the studied problem under multi-frequency half-sinusoidal heating (temperature) are analyzed and illustrated in Fig. 15 for different frequencies f ($= 1, 3, 5, 10$) for different values of Ra_m , Da, I , Ha, and ϕ . Figure 15a depicts the variation in the average Nu with the variation in Ra_m for the fixed values of $Da = 10^{-4}$, $I=1$, $Ha=30$, $\phi=0.02$. At the lower value of Ra_m , the conduction mode drives the fluid flow, resulting in

weaker fluid circulation in the enclosure and lower average Nu. However, for the $Ra_m \geq 10^2$, thermal convection mode dominates the conduction mode; thus, consistently increasing Nu is observed irrespective of any frequency f . Interestingly, at lower Ra_m value up to < 120 (estimated point), higher frequency mode is found to be more advantageous compared to the case of single frequency, and beyond this point low frequency is always found to be superior.

The increase in the permeability of the porous media on the overall thermal performance is illustrated in Fig. 15b for the different $Ra_m = 10^3$, $I=1$, $Ha=30$, $\phi=0.02$. As Da ($=Ra_m/Ra$) value increases for the fixed Ra_m , the fluid-based Ra decreases. As a result, the decreasing trend of Nu with increasing Da is observed for any frequency f . As Ra is significantly low, the enhanced permeability of the porous media has no influence on the average Nu. This is an interesting finding over the existing notion of an increasing trend of Nu with increasing Da. Furthermore, the low frequency is always found to be superior up to $Da > 10^{-3}$; beyond this, the higher frequency mode is found to be more advantageous as reflected by the Nu curve.

For the multi-frequency half-sinusoidal heating, the amplitude (I) is also an important factor for modulating the thermal performance. Figure 15c illustrates the effect of varying I for different frequencies f considering $Ra_m = 10^3$, $Da = 10^{-4}$, $Ha=30$, $\phi=0.02$. The average Nu increases monotonically with increasing I for any frequency value. The low frequency is found to be superior after $I=0.3$ compared to that of higher frequency mode as reflected by the Nu curve. At the lower amplitude, the thermal convection is very weak as a result of lower local temperature at the heated wall (as shown in Fig. 12b). The above findings are also supported by the earlier findings as shown in Figs. 5 and 14c.

The effect of externally applied magnetic field strength on the overall thermal performance is illustrated in Fig. 15d for different Ha values at $Ra_m = 10^3$, $Da = 10^{-4}$, $I=1$, $\phi=0.02$. The average Nu decreases with increasing Ha. An increase in an imposed magnetic field causes a reduction in the fluid velocity and, in turn, inhibits the convective heat transfer (as shown in Fig. 9). Furthermore, low frequency f reflects a higher rate of heat transfer characteristics. Figure 15e illustrates the effect of different volume fractions of Cu–Al₂O₃/water hybrid nanofluid on overall thermal behavior at $Ra_m = 10^3$, $Da = 10^{-4}$, $I=1$, $Ha=30$. The addition of Cu–Al₂O₃ nanoparticles escalates the effective thermal conductivity of the fluid, resulting buoyancy force becomes stronger. Thus, the average Nu increases irrespective of any frequency f . As ϕ increases beyond 0.0033, it is seen that circulation strength reduces (as shown in Fig. 10). This is attributed due to the increase in the viscosity of the hybrid nanofluid. Thus, the resistance to the fluid flow increases besides the buoyancy force, as the dynamic viscosity of

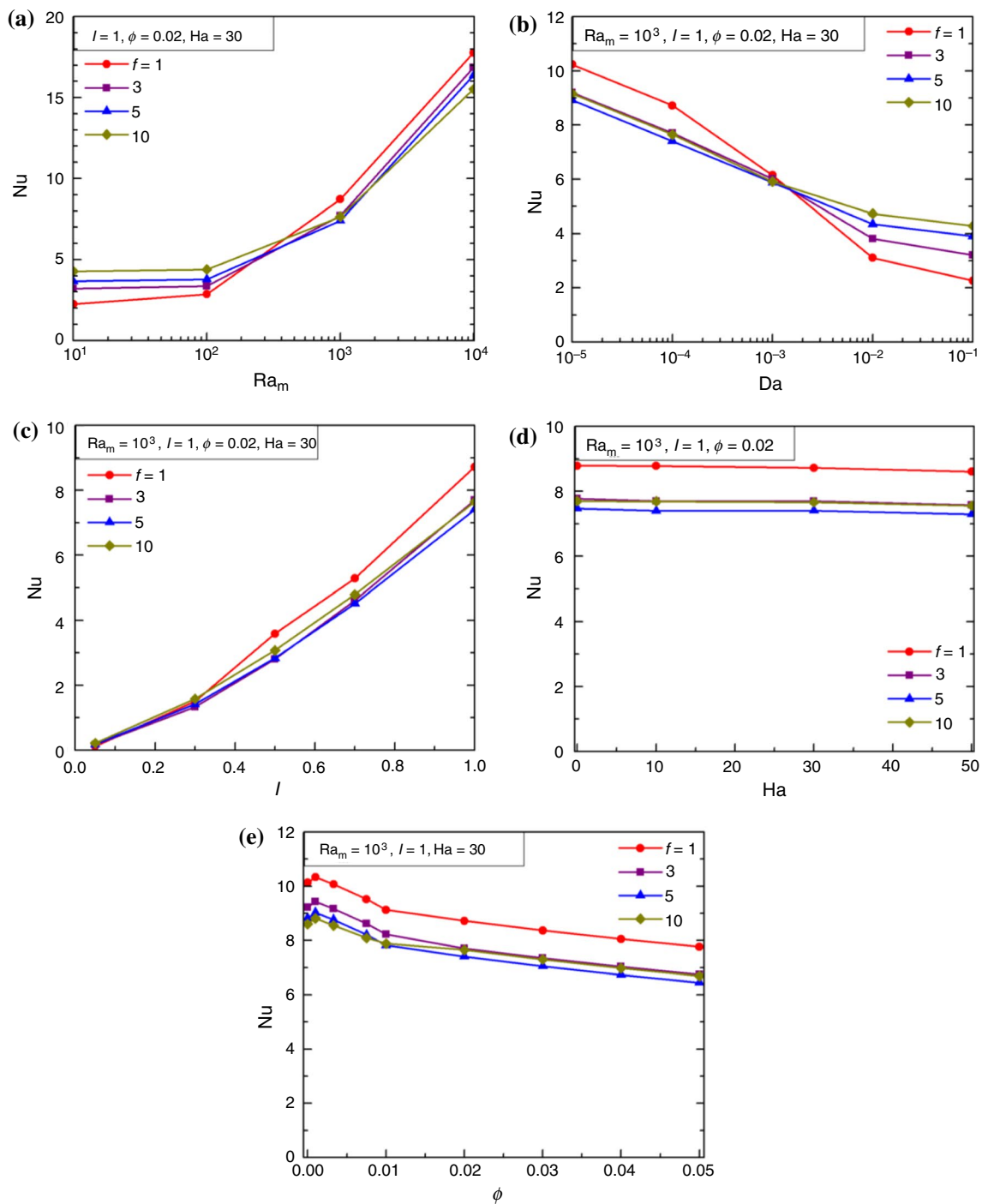


Fig. 15 (Color figure online) Heat transfer characteristics with varying, **a** Darcy–Rayleigh number (Ra_m), **b** Darcy number (Da), **c** amplitude (l) of half-sinusoidal heating (temperature), **d** Hartmann number (Ha), **e** Cu–Al₂O₃ hybrid nanoparticles concentration (ϕ)

the hybrid nanofluid increases. Further increase in ϕ leads to a decrease in the average Nu monotonically. In this case also, the low frequency of half-sinusoidal heating is always found to be superior. Further to the above,

during the analysis, it is also observed that at lower values of Ra_m ($< 10^2$) the presence of Cu–Al₂O₃ nanoparticles causes a significant improvement in the average Nu compared to the pure fluid.

Conclusions

Significance and fundamental flow physics of hybrid nanofluid saturated with porous media under the effect of multi-frequency half-sinusoidal heating at the bottom of an enclosure in the presence of a magnetic field are analyzed numerically and presented in this study. The enclosure is isothermally cooled at the sides, and the top wall is insulated. The effects of pertinent parameters, such as Darcy–Rayleigh number, Darcy number, amplitude and frequency of half-sinusoidal heating, Hartmann number and hybrid nanoparticles concentrations, are investigated thoroughly. The salient outcomes of this study are summarized below:

- The amplitude and frequency of applied half-sinusoidal heating strongly modulate the natural convective heat transfer process. The half-sinusoidal heating with lower frequency can be a superior heating strategy at a higher value of $Ra_m > 10^2$. Higher frequency is only advantageous for the lower range of $Ra_m (\leq 10^2)$. In addition, both the circulation strength and average Nu are higher at the higher value of Ra_m .
- With the increase in the frequency of half-sinusoidal heating beyond $f=1$ (up to 10), simultaneous heating and cooling take place at the heated wall, resulting in the periodic oscillation of the local temperature as well as local and average Nu. Heat transfer rate decreases with increasing frequency due to the presence of such an intermediate cooling effect.
- The multi-frequency spatial heating amplitude (I) also plays a crucial role in the overall thermo-fluid flow behavior. An increase in the amplitude leads to an increase in the heat transfer rate monotonically and becomes maximum at higher amplitude $I=1$ and higher Ra_m .
- As Ra_m increases, more depression in the local Nu profile is noted about the central point of the bottom wall. This is attributed due to the formation of a stagnation zone over a certain horizontal portion near the heated wall, leading to a reduction in localized heat transfer from the heated wall. As a result, a sharp fall in the local Nu around $X=0.5$ is noted. This is an interesting finding of this case study.
- The convective heat transfer of hybrid nanofluid is strongly affected by the permeability of the porous media. For the fixed values of $Ra_m (=Ra \times Da)$, an increase in Da results in a decrement of overall heat transfer rate, which contradicts the usual notion. The increase in Da corresponds to a decrement in the fluid-based Ra ; it reduces the intensity of thermal convection as well as average Nu. This is also another interesting finding in this study.

- Addition of Cu–Al₂O₃ hybrid nanoparticles into the pure water does not always improve the heat transfer rate. The addition of Cu–Al₂O₃ nanoparticles enhances the effective thermal conductivity of the fluid; thus, the resistance to the fluid flow reduces, and the average Nu increases irrespective of any frequency f . As ϕ increases beyond 0.0033, the viscosity of the hybrid nanofluid increases, leading to a decrement in the average Nu monotonically. It is also observed that at lower values of $Ra_m (< 10^2)$ the presence of Cu–Al₂O₃ nanoparticles causes a significant improvement in the average Nu compared to the pure fluid.
- When the externally applied magnetic field strength (in terms of Ha) increases, the thermal buoyancy decreases, resulting in a decrease in the heat transfer rate monotonically irrespective of any f , I , Ra_m and ϕ .
- Thermal energy transports from the heat source to the heat sink under various thermal conditions are visualized using Bejan's heatlines.

The results show that the multi-frequency half-sinusoidal nonuniform heating along with the hybrid nanofluid can be useful for controlling the overall thermal performance of a system even in the presence of flow dampening effects like porous media and magnetic fields. The findings of this study can easily be accommodated during the modeling, designing, and controlling thermo-fluid behavior of relevant thermal devices.

Compliance with ethical standards

Conflict of interest All authors declare that they have no conflict of interest.

References

1. Incropera FP. Convection heat transfers in electronic equipment cooling. *J Heat Transf.* 1988;110:1097–111.
2. Remsburg R. Thermal design of electronic equipment. Boca Raton: CRC Press LLC; 2001.
3. Nield DA, Bejan A. Convection in porous media. 3rd ed. Berlin: Springer; 2006.
4. Rehman T, Ali HM, Janjua MM, Sajjad U, Yan W-M. A critical review on heat transfer augmentation of phase change materials embedded with porous materials/foams. *Int J Heat Mass Transf.* 2019;135:649–73.
5. Bagchi A, Kulacki FA. Natural convection in superposed fluid-porous layers. London: Springer; 2014.
6. Garimella SV, Persoons T, Weibel JA, Gektin V. Electronics thermal management in information and communications technologies: challenges and future directions. *IEEE Trans Comp Pack Manuf Technol.* 2016;PP:1–15.
7. Manna NK, Biswas N, Mahapatra PS. Convective heat transfer enhancement: effect of multi-frequency heating. *Int J Numer Methods Heat Fluid Flow.* 2019;2019:0961–5539.

8. Chakravarty A, Biswas N, Ghosh K, Manna NK, Mukhopadhyay A, Sen S. Impact of side injection on heat removal from truncated conical heat-generating porous bed: thermal non-equilibrium approach. *J Therm Anal Calorim.* 2020. <https://doi.org/10.1007/s10973-020-09295-6>.
9. Rehman T, Ali HM. Thermal performance analysis of metallic foam-based heat sinks embedded with RT-54HC paraffin: an experimental investigation for electronic cooling. *J Therm Anal Calorimetry.* 2020;140:979–90.
10. Rehman T, Ali HM. Experimental study on the thermal behavior of RT-35HC paraffin within copper and Iron-Nickel open cell foams: energy storage for thermal management of electronics. *Int J Heat Mass Transf.* 2020;146:118852.
11. Rehman T, Ali HM. Experimental investigation on paraffin wax integrated with copper foam based heat sinks for electronic components thermal cooling. *Int Commun Heat Mass Transf.* 2018;98:155–62.
12. Rehman T, Ali HM, Saieed A, Pao W, Ali M. Copper foam/PCMs based heat sinks: an experimental study for electronic cooling systems. *Int J Heat Mass Transf.* 2018;127:381–93.
13. Sajawal M, Rehman T, Ali HM, Sajjad U, Raza A, Bhatti MS. Experimental thermal performance analysis of finned tube-phase change material based double pass solar air heater. *Case Stud Thermal Eng.* 2019;15:100543.
14. Choi SU, Eastman JA. Enhancing thermal conductivity of fluids with nanoparticles. Lemont: Argonne National Lab; 1995.
15. Kahveci K. Buoyancy driven heat transfer of nanofluids in a tilted enclosure. *J Heat Transf.* 2010;132(6):062501.
16. Babar H, Ali HM. Airfoil shaped pin-fin heat sink: potential evaluation of ferric oxide and titania nanofluids. *Energy Conv Manag.* 2019;202:112194-1–19.
17. Sajid MU, Ali HM, Sufyan A, Rashid D, Zahid SU, Rehman WU. Experimental investigation of TiO₂–water nanofluid flow and heat transfer inside wavy mini-channel heat sinks. *J Therm Anal Calorim.* 2019;137:1279–94.
18. Khanafer K, Vafai K. Applications of nanofluids in porous medium. *J Therm Anal Calorim.* 2019;135:1479–92.
19. Kasaeian A, Daneshzarian R, Mahian O, Kolsi L, Chamkha AJ, Wongwises S, Pop I. Nanofluid flow and heat transfer in porous media: a review of the latest developments. *Int J Heat Mass Transf.* 2017;107:778–91.
20. Rahimi A, Saeed AD, Kasaeipoor A, Malekshah EH. A comprehensive review on natural convection flow and heat transfer: the most practical geometries for engineering applications. *Int J Numer Methods Heat Fluid Flow.* 2019;29(3):834–77.
21. Nazari MA, Ghasempour R, Ahmadi MH. A review on using nanofluids in heat pipes. *J Therm Anal Calorim.* 2019;137:1847–55.
22. Prakash J, Siva EP, Tripathi D, Bég OA. Thermal slip and radiative heat transfer effects on electro-osmotic magnetonanoliquid peristaltic propulsion through a microchannel. *Heat Transf Asian Res.* 2019;48:2882–908.
23. Prakash J, Siva EP, Tripathi D, Kuharat S, Bég OA. Peristaltic pumping of magnetic nanofluids with thermal radiation and temperature-dependent viscosity effects: modelling a solar magnetobiomimetic nanopump. *Renew Energy.* 2019;133:1308–26.
24. Prakash J, Sharma A, Tripathi D. Convective heat transfer and double diffusive convection in ionic nanofluids flow driven by peristalsis and electromagnetohydrodynamics. *Pramana J Phys.* 2020;94:14–7.
25. Narla VK, Tripathi D, Bég OA. Analysis of entropy generation in biomimetic electroosmotic nanofluid pumping through a curved channel with joule dissipation. *Thermal Sci Eng Prog.* 2020;15:100424.
26. Sajid MU, Ali HM. Recent advances in application of nanofluids in heat transfer devices: a critical review. *Renew Sus Energy Rev.* 2019;103:556–92.
27. Soudagar MEM, Kalam MA, Sajid MU, Afzal A, Banapurmath NR, Akram N, Mane SD, Ahamed Saleel C. Thermal analyses of minichannels and use of mathematical and numerical models. *Numer Heat Transf A.* 2020;77(5):497–537.
28. Wahab A, Hassan A, Qasim MA, Ali HM, Babar H, Sajid MU. Solar energy systems—potential of nanofluids. *J Mol Liq.* 2019;289:111049.
29. Ali HM, Babar H, Shah TR, Sajid MU, Qasim MA, Javed S. Preparation techniques of TiO₂ nanofluids and challenges: a review. *Appl Sci.* 2018;8(587):1–30.
30. Babar H, Sajid MU, Ali HM. Viscosity of hybrid nanofluids a critical review. *Therm Sci.* 2019;23(3B):1713–54.
31. Sarkar J, Ghosh P, Adil A. A review on hybrid nanofluids: recent research, development and applications. *Renew Sustain Energy Rev.* 2015;43:164–77.
32. Bhosale GH, Borse SL, Pool Boiling CHF. Enhancement with Al₂O₃–CuO/H₂O hybrid nanofluid. *Int J Eng Res Technol.* 2013;2(10):946–50.
33. Selvakumar P, Suresh S. Use of Al₂O₃–Cu/water hybrid nanofluid in an electronic heat sink. *IEEE Trans Compon Package Manuf Technol.* 2012;2(10):1600–7.
34. Sajid MU, Ali HM. Thermal conductivity of hybrid nanofluids: a critical review. *Int J Heat Mass Transf.* 2018;126:211–34.
35. Prakash J, Siva EP, Tripathi D, Bég OA. Comparative study of hybrid nanofluids in microchannel slip flow induced by electroosmosis and peristalsis. *Appl Nanosci.* 2020;10:1693–706.
36. Suresh S, Venkitaraj K, Selvakumar P, Chandrasekar M. Effect of Al₂O₃–Cu/water hybrid nanofluid in heat transfer. *Exp Therm Fluid Sci.* 2012;38:54–60.
37. Ghalambaz M, Mehryan SAM, Izadpanahi E, Chamkha AJ, Wen D. MHD natural convection of Cu–Al₂O₃ water hybrid nanofluids in a cavity equally divided into two parts by a vertical flexible partition membrane. *J Therm Anal Calorim.* 2019;138:1723–43.
38. Ghalambaz M, Sheremet MA, Mehryan SAM, Kashkooli FM, Pop I. Local thermal non-equilibrium analysis of conjugate free convection within a porous enclosure occupied with Ag–MgO hybrid nanofluid. *J Therm Anal Calorim.* 2019;135:1381–98.
39. Chamkha AJ, Sazegar S, Jamesahar E, Ghalambaz M. Thermal non-equilibrium heat transfer modeling of hybrid nanofluids in a structure composed of the layers of solid and porous media and free nanofluids. *Energies.* 2019;12:541.
40. Al-Srayyih BM, Gao S, Hussain SH. Natural convection flow of a hybrid nanofluid in a square enclosure partially filled with a porous medium using a thermal non-equilibrium model. *Phys Fluids.* 2019;31:043609.
41. Mehryan SAM, Sheremet MA, Soltani M, Izadi M. Natural convection of magnetic hybrid nanofluid inside a double-porous medium using two-equation energy model. *J Mol Liq.* 2019;277:959–70.
42. Izadi M, Mohebbi R, Delouei AA, Sajjadi H. Natural convection of a magnetizable hybrid nanofluid inside a porous enclosure subjected to two variable magnetic fields. *Int J Mech Sci.* 2018;151:154–69.
43. Mansour MA, Siddiqi S, Gorla RSR, Rashad AM. Effects of heat source and sink on entropy generation and MHD natural convection of Al₂O₃–Cu/water hybrid nanofluid filled with square porous cavity. *Therm Sci Eng Prog.* 2018;6:57–71.
44. Ghadikolaei SS, Hosseinzadeh Kh, Hatami M, Ganji DD. MHD boundary layer analysis for micropolar dusty fluid containing Hybrid nanoparticles (CuAl₂O₃) over a porous medium. *J Mol Liq.* 2018;268:813–23.
45. Ghadikolaei SS, Gholinia M. Terrific effect of H₂ on 3D free convection MHD flow of C₂H₆O₂–H₂O hybrid base fluid to dissolve Cu nanoparticles in a porous space considering the thermal radiation and nanoparticle shapes effects. *Int J Hydrog Energy.* 2019;44:17072–83.

46. Mehryan SAM, Izadi M, Namazian Z, Chamkha Ali J. Natural convection of multi-walled carbon nanotube- Fe_3O_4 /water magnetic hybrid nanofluid flowing in porous medium considering the impacts of magnetic field-dependent viscosity. *J Therm Anal Calorim.* 2019;138:1541–55.
47. Biswas N, Mahapatra PS, Manna NK. Merit of non-uniform over uniform heating in a porous cavity. *Int J Heat Mass Transf.* 2016;78:135–44.
48. Saeid NF. Natural convection in porous cavity with sinusoidal bottom wall temperature variation. *Int Commun Heat Mass Transf.* 2005;32:454–63.
49. Khandelwal MK, Bera P, Chakrabarti A. Influence of periodicity of sinusoidal bottom boundary condition on natural convection in porous enclosure. *Int J Heat Mass Transf.* 2012;55:2889–900.
50. Chandra H, Bera P, Sharma AK. Natural convection in a square cavity filled with an anisotropic porous medium due to sinusoidal heat flux on horizontal walls. *Numer Heat Transf A.* 2020;77(3):317–41.
51. Wu F, Wang G, Zhou W. Buoyancy induced convection in a porous cavity with sinusoidally and partially thermally active sidewalls under local thermal non-equilibrium condition. *Int Commun Heat Mass Transf.* 2016;75:100–14.
52. Cimpean DS, Revnic C, Pop I. Natural convection in a square inclined cavity filled with a porous medium with sinusoidal temperature distribution on both side walls. *Transp Porous Med.* 2019;130:391–404.
53. Oztop HF, Abu-Nada E, Varol Y, Al-Salem K. Computational analysis of nonisothermal temperature distribution on natural convection in nanofluid filled enclosures. *Super Micro.* 2011;49:453–67.
54. Mikhailenko SA, Sheremet MA, Pop I. Convective heat transfer in a rotating nanofluid cavity with sinusoidal temperature boundary condition. *J Therm Anal Calorim.* 2019;137:799–809.
55. Alsabery AI, Chamkha AJ, Saleh H, Hashim I, Chanane B. Effects of finite wall thickness and sinusoidal heating on convection in nanofluid-saturated local thermal non-equilibrium porous cavity. *Physica A.* 2017;470:20–38.
56. Arasteh H, Mashayekhi R, Goodarzi M, Motaharpour SH, Dahari M, Toghraie D. Heat and fluid flow analysis of metal foam embedded in a double-layered sinusoidal heat sink under local thermal non-equilibrium condition using nanofluid. *J Therm Anal Calorim.* 2019;138:1461–76.
57. Li Z, Shehzad SA, Sheikholeslami M. An application of CVFEM for nanofluid heat transfer intensification in a porous sinusoidal cavity considering thermal non-equilibrium model. *Comput Methods Appl Mech Eng.* 2018;339:663–80.
58. Aly AM, Ahmed SE, Raizah ZAS. Double-diffusive natural convection in a square porous cavity with sinusoidal distributions sidewalls filled with a nanofluid. *J Porous Med.* 2018;21(2):101–22.
59. Al-Amir QR, Ahmed SY, Hamzah HK, Ali FH. Effects of Prandtl number on natural convection in a cavity filled with silver/water nanofluid-saturated porous medium and non-Newtonian fluid layers separated by sinusoidal vertical interface. *Arab J Sci Eng.* 2019;44:10339–54.
60. Sheremet MA, Pop I. Natural convection in a square porous cavity with sinusoidal temperature distributions on both side walls filled with a nanofluid: Buongiorno's mathematical model. *Transp Porous Med.* 2014;105:411–29.
61. Malik S, Nayak AK. MHD convection and entropy generation of nanofluid in a porous enclosure with sinusoidal heating. *Int J Heat Mass Transf.* 2017;111:329–45.
62. Nazeer M, Ali N, Javed T. Numerical simulation of MHD flow of micropolar fluid inside a porous inclined cavity with uniform and non-uniform heated bottom wall. *Can J Phys.* 2018;96:576–93.
63. Javaherdeh K, Najjarnezami A. Lattice Boltzmann simulation of MHD natural convection in a cavity with porous media and sinusoidal temperature distribution. *Appl Math Mech Engl Ed.* 2018;39(8):1187–200.
64. Pordanjani AH, Jahanbakhshi A, Nadooshan AA, Afrand M. Effect of two isothermal obstacles on the natural convection of nanofluid in the presence of magnetic field inside an enclosure with sinusoidal wall temperature distribution. *Int J Heat Mass Transf.* 2018;121:565–78.
65. Vo DD, Shah Z, Sheikholeslami M, Shafee A, Nguyen TK. Numerical investigation of MHD nanomaterial convective migration and heat transfer within a sinusoidal porous cavity. *Phys Scr.* 2019;94:115225–1–10.
66. Aly AM, Raizah ZAS. Incompressible smoothed particle hydrodynamics method for natural convection of a ferrofluid in a partially layered porous cavity containing a sinusoidal wave rod under the effect of a variable magnetic field. *AIP Adv.* 2019;9:105210-1–21.
67. Tayebi T, Chamkha AJ. Buoyancy-driven heat transfer enhancement in a sinusoidally heated enclosure utilizing hybrid nanofluid. *Comput Therm Sci.* 2017;9(5):405–21.
68. Takabi B, Salehi S. Augmentation of the heat transfer performance of a sinusoidal corrugated enclosure by employing hybrid nanofluid. *Adv Mech Eng.* 2014;6:147059.
69. Ashorynejad HR, Shahriari A. MHD natural convection of hybrid nanofluid in an open wavy cavity. *Results Phys.* 2018;9:440–55.
70. Ghalambaz M, Doostani A, Izadpanahi E, Chamkha AJ. Conjugate natural convection flow of Ag-MgO/water hybrid nanofluid in a square cavity. *J Therm Anal Calorim.* 2020;139:2321–36.
71. Almeshaal MA, Kalidasan K, Askri F, Velkenedy R, Alsagri AS, Kolsi L. Three-dimensional analysis on natural convection inside a T-shaped cavity with water-based CNT-aluminum oxide hybrid nanofluid. *J Therm Anal Calorim.* 2020;139:2089–98.
72. Tayebi T, Chamkha AJ. Entropy generation analysis due to MHD natural convection flow in a cavity occupied with hybrid nanofluid and equipped with a conducting hollow cylinder. *J Therm Anal Calorim.* 2020;139:2165–79.
73. Abdel-Nour Z, Aissa A, Mebarek-Oudina F, Rashad AM, Ali HM, Sahnoun M, Ganaoui ME. Magnetohydrodynamic natural convection of hybrid nanofluid in a porous enclosure: numerical analysis of the entropy generation. *J Therm Anal Calorim.* 2020. <https://doi.org/10.1007/s10973-020-09690-z>.
74. Babazadeh H, Shah Z, Ullah I, Kumam P, Shafee A. Analysis of hybrid nanofluid behavior within a porous cavity including Lorentz forces and radiation impacts. *J Therm Anal Calorim.* 2020. <https://doi.org/10.1007/s10973-020-09416-1>.
75. Manh TD, Nam ND, Abdulrahman GK, Moradi R, Babazadeh H. Impact of MHD on hybrid nanomaterial free convective flow within a permeable region. *J Therm Anal Calorim.* 2020;140:2865–73.
76. Biswas N, Manna NK. Enhanced convective heat transfer in lid-driven porous cavity with aspiration. *Int J Heat Mass Transf.* 2019;114:430–52.
77. Biswas N, Manna NK, Datta P, Mahapatra PS. Analysis of heat transfer and pumping power for bottom-heated porous cavity saturated with Cu-water nanofluid. *Powder Technol.* 2018;326:356–69.
78. Incropera FP, DeWitt DP. Introduction to heat transfer. New York: Wiley; 2002.
79. Brinkman JH. The viscosity of concentrated suspensions and solutions. *J Chem Phys.* 1952;20(4):571.
80. Maxwell JC. A treatise on electricity and magnetism. Oxford: Clarendon Press; 1881.
81. Patankar SV. Numerical heat transfer and fluid flow. New York: Hemisphere; 1980.

82. Biswas N, Mahapatra PS, Manna NK, Roy PC. Influence of heater aspect ratio on natural convection in a rectangular enclosure. *Heat Transf Eng.* 2016;37(2):125–39.
83. Biswas N, Manna NK. Magneto-hydrodynamic Marangoni flow in bottom-heated lid-driven cavity. *J Mol Liq.* 2018;251:249–66.
84. Biswas N, Manna NK, Mahapatra PS. Enhanced thermal energy transport using adiabatic block inside lid-driven cavity. *Int J Heat Mass Transf.* 2016;100:407–27.
85. Ghasemi B, Aminossadati SM, Raisi A. Magnetic field effect on natural convection in a nanofluid-filled square enclosure. *Int J Therm Sci.* 2011;50:1748–56.

Publisher's Note Springer Nature remains neutral with regard to jurisdictional claims in published maps and institutional affiliations.

Affiliations

Nirmalendu Biswas¹  · U. K. Sarkar²  · Ali J. Chamkha^{3,4}  · Nirmal Kumar Manna⁵ 

Nirmalendu Biswas
nirmalendubiswas@yahoo.co.in

U. K. Sarkar
rahi_utu@yahoo.co.in

Ali J. Chamkha
alichamkha@duytan.edu.vn

¹ Department of Power Engineering, Jadavpur University, Salt Lake, Kolkata 700106, India

² Department of Mechanical Engineering, Techno Main Salt Lake, Kolkata 700098, India

³ Institute of Research and Development, Duy Tan University, Da Nang 550000, Vietnam

⁴ Institute of Theoretical and Applied Research (ITAR), Duy Tan University, Hanoi 100000, Vietnam

⁵ Department of Mechanical Engineering, Jadavpur University, Kolkata 700032, India